THE GEOLOGICAL SOCIETY OF AMERICA®

Tephra zircon U-Pb geochronology of kimberlite maar sedimentary fills in subarctic Canada: Implications for Eocene paleoclimate and Late Cretaceous paleogeography

Serhiy D. Buryak[1,†], Alberto V. Reyes[1], Christopher K. West[1,2], Britta J.L. Jensen[1], S. Andrew DuFrane[1], Joshua H.F.L. Davies[3], Yan Luo[1], Jennifer M. Galloway[4], Peter A. Siver[5], John A. Westgate[6], Jesse R. Reimink[7], D. Graham Pearson[1], and Alexander P. Wolfe[1]

[1]*Department of Earth and Atmospheric Sciences, University of Alberta, Edmonton, Alberta T6G 2E3, Canada*
[2]*Royal Tyrrell Museum of Palaeontology, Box 7500, Drumheller, Alberta T0J 0Y0, Canada*
[3]*Département des Sciences de la Terre et de l'Atmosphère/GEOTOP, Université du Québec à Montréal, Montréal, Québec H2X 3Y7, Canada*
[4]*Geological Survey of Canada/Commission géologique du Canada, 3303-33 Street N.W., Calgary, Alberta T2L 2A7, Canada*
[5]*Department of Botany, Connecticut College, New London, Connecticut 06320, USA*
[6]*Department of Earth Sciences, University of Toronto, Toronto, Ontario M5S 3B1, Canada*
[7]*Department of Geosciences, Pennsylvania State University, University Park, Pennsylvania 16802, USA*

ABSTRACT

The Wombat and Giraffe kimberlite pipes in the Lac de Gras kimberlite field (64°N, 110°W) of the Northwest Territories, Canada, preserve unique post-eruptive lacustrine and paludal sedimentary records that offer rare insight into high-latitude continental paleoclimate. However, depositional timing—a key datum for atmospheric CO_2 and paleoclimatic proxy reconstructions—of these maar infills remains ambiguous and requires refinement because of the large range in the age of kimberlites within the Lac de Gras kimberlite field. Existing constraints for the Giraffe pipe post-eruptive lacustrine and paludal maar sedimentary facies include a maximum Rb-Sr age of ca. 48 Ma (Ypresian, Eocene) based on kimberlitic phlogopite and a glass fission-track age of ca. 38 Ma (Bartonian, Eocene). The age of the Wombat pipe lacustrine maar sediments remains unclear, with unpublished pollen-based biostratigraphy suggesting deposition in the Paleocene (66–56 Ma). In this study, we examine distal rhyolitic tephra beds recovered from exploration drill cores intersecting the Wombat and Giraffe maar facies. We integrate zircon U-Pb laser ablation–inductively coupled plasma–mass spectrometry (LA-ICP-MS) and chemical abrasion–isotope dilution–thermal ionization mass spectrometry (CA-ID-TIMS) geochronology, glass fission-track dating, palynology, and tephra glass geochemistry to refine chronological frameworks for these sedimentary deposits. The Giraffe maar CA-ID-TIMS tephra zircon U-Pb dating yielded a Bayesian model age of 47.995 ± 0.082|0.087 Ma (Ypresian) for the upper portion of the lacustrine sediments, while a single zircon grain from tephra in the lowermost lacustrine sediments had an age of 48.72 ± 0.29|0.30 Ma. The revised geochronology for the Giraffe maar provides a working age model for the ~50 m record of lacustrine silt and indicates an age ~10 m.y. older than previously thought. The Wombat maar LA-ICP-MS zircon U-Pb dating yielded an age of 80.9 ± 1.0 Ma (Campanian), which indicates deposition during the Late Cretaceous. This first radiometric age for the Wombat maar deposits is substantially older than earlier biostratigraphic inferences of a Paleocene age. This new age suggests that the Wombat maar sediments preserve evidence of some of the oldest known freshwater diatoms and synurophytes and provide key constraints for the paleogeography of the Western Interior Seaway during the Late Cretaceous.

1. INTRODUCTION

Kimberlites are CO_2- and water-rich ultramafic volcanic rocks that were emplaced during highly volatile phreatomagmatic eruptions, leading to the formation of broadening diatremes and—under exceptional circumstances—post-eruptive craters and maar lakes (Nowicki et al., 2004; Giuliani and Pearson, 2019). In a small but relatively deep (>80 m) kimberlitic maar lake, bottom-water anoxic conditions can develop to facilitate preservation of sedimentary organic matter and fossils. As a result, maar lake sediments can be excellent sources of paleoenvironmental records because they typically provide continuous and well-preserved sedimentary successions (e.g., Sabel et al., 2005; Hamblin, 2015; Smith et al., 2018; Siver and Lott, 2023).

Despite their potential for paleoenvironmental study, kimberlite maar lake sediments have received relatively little attention. Notable kimberlite maar lake records include the Star in Canada, Orapa in Botswana, Mwadui in Tanzania, and Mbuji Mayi in Congo (Edwards and Howkins, 1966; Hawthorne, 1975; Nixon, 1995; Field et al., 1995; Stiefenhofer and Farrow, 2003; Zonneveld et al., 2004). Some lamproite pipes are also known to host post-eruptive maar lake sediments, including the Argyle lamproite pipe (Boxer et al., 1986) and the Calwynyardah lamproite maars in Western Australia (Jaques et al., 1986).

Kimberlite maar lake sediments are also present in the Lac de Gras kimberlite field in northern Canada (Nowicki et al., 2004). The most prominent examples of maar lake deposits in this field are associated with the Giraffe and Wombat kimberlite pipes (Fig. 1), although lacustrine facies are also known from the Sue and A154N pipes (Nassichuk and Dyck, 1998; Moss et al., 2008).

Alberto V. Reyes https://orcid.org/0000-0002-7838-4214
†buryak@ualberta.ca

GSA Bulletin; https://doi.org/10.1130/B37276.1.

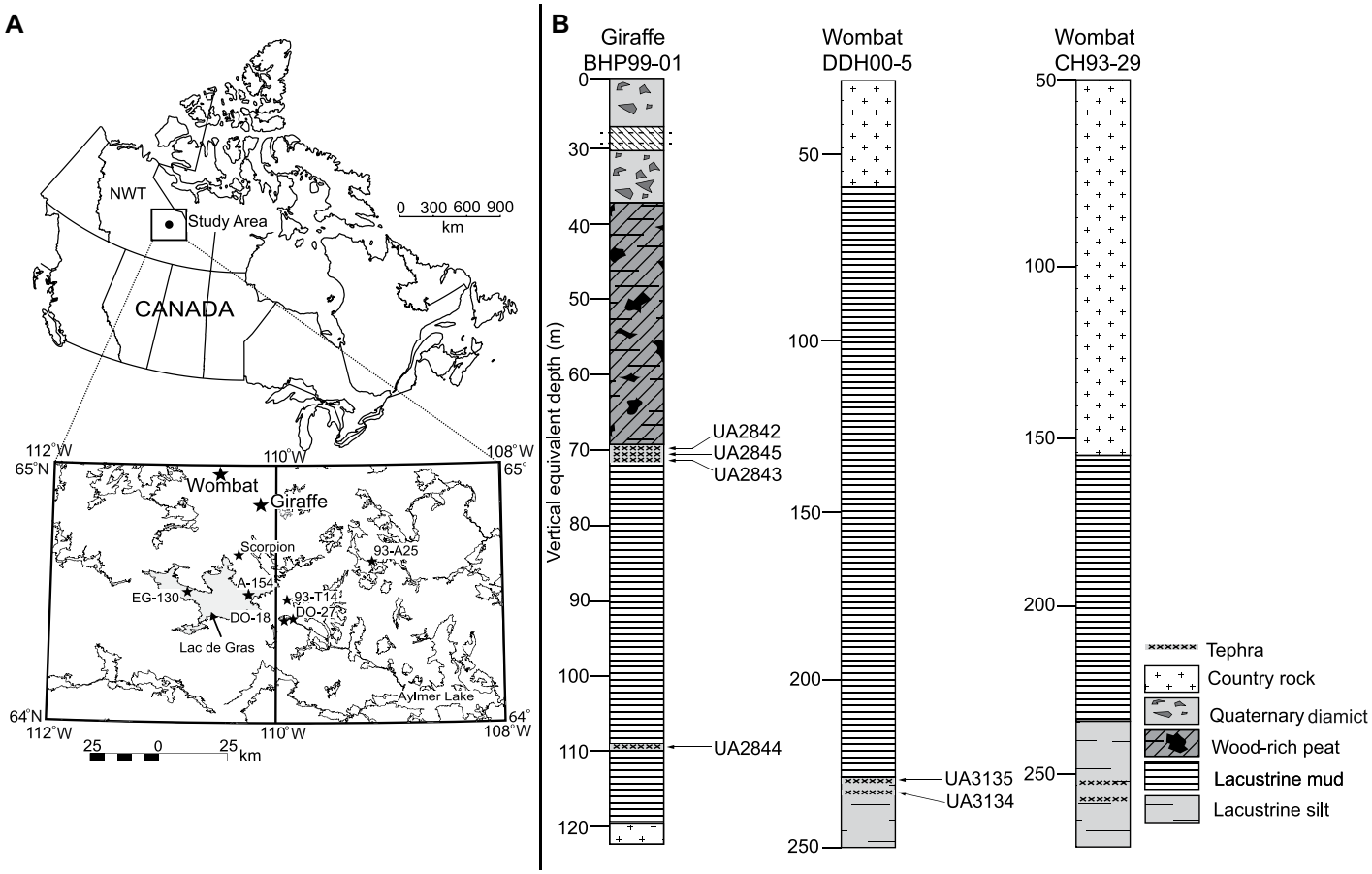

Figure 1. (A) Map of the Wombat and Giraffe pipe localities and locations of other kimberlites in the Lac de Gras area, Northwest Territories (NWT), Canada (adapted from Stasiuk et al., 2002). (B) Stratigraphic log summaries of Giraffe drill core BHP99-01 and Wombat drill cores DDH00-5 and CH93-29. Sample locations of the tephra layers are marked with arrows. Depth in the dipping cores is expressed as vertical equivalent depth with respect to the modern surface.

The Giraffe kimberlite locality, which is the most well-known of the Lac de Gras kimberlite maars, hosts a unique lacustrine and paludal sedimentary record deposited during the Eocene epoch (e.g., Stasiuk et al., 2002; Hamblin et al., 2003; Doria et al., 2011; Hamblin, 2015; Wolfe et al., 2017). The Giraffe maar sediments and peat provide a unique window into terrestrial paleoenvironments of the early Cenozoic greenhouse world, in a region of subarctic Canada that is otherwise largely devoid of pre-Quaternary sedimentary cover. Additionally, an extensive array of microfossils recovered from the Giraffe maar lake deposits—including diatoms, chrysophytes, synurophytes, euglyphids, heliozoans, and sponges—provides further insight into paleoenvironmental conditions in the region (e.g., Barber et al., 2013; Pisera et al., 2013; Siver, 2015; Siver et al., 2019; Siver and Lott, 2023).

The geochronology of the Giraffe paleoenvironmental record remains uncertain. An Rb-Sr model age of 47.8 ± 1.4 Ma from kimberlitic phlogopite provides a maximum age for maar lake sedimentation (Creaser et al., 2004). Four glass fission-track age determinations on two rhyolitic tephra horizons in the uppermost Giraffe maar lake sediments, using diameter-corrected and isothermal plateau methods to correct for partial track fading (Westgate, 2015), yielded an error-weighted mean age of 37.8 ± 4.0 Ma (2σ) for the transition from maar lacustrine facies to paludal peat facies (Doria et al., 2011; Wolfe et al., 2017). The ~10 m.y. difference between the Rb-Sr emplacement age and the glass fission-track age constraint for lacustrine sedimentation is problematic. Even allowing for a substantial lag between kimberlite eruption and the onset of lacustrine conditions in the maar, ~50 m of lacustrine sediment and ~30 m of peat deposited over ~5–10 m.y. implies implausibly low sedimentation rates. In addition, the magnitude of the glass fission-track corrections for partial track fading (~10 m.y.; Wolfe et al., 2017) introduces substantial uncertainty into the geochronology of this deposit.

Similar kimberlite diatreme maar lake deposits are present at the Wombat locality, which is ~40 km NW of the Giraffe pipe (Fig. 1). The Wombat pipe post-eruptive sedimentary fill is thick and homogenous; three exploration drill cores intersect the pipe over 195 vertical-equivalent (VE) meters and contain mostly laminated lacustrine sediment. These sediments host exceptionally well-preserved microfossil and macrofossil remains (Siver et al., 2016; Siver, 2022; Grande et al., 2022; Siver and Velez, 2023). The Wombat maar sediments contain abundant siliceous microfossils, including chrysophyte cysts, scales representing synurophytes, chrysophytes, and heliozoans, and a variety of pennate and centric diatoms, all of which are indicative of a freshwater lacustrine environment (Fig. 2; Siver et al., 2016; Siver, 2022). In addition, a new Gonorynchiform fossil fish species, *Notogoneus maarvelis*, sp. nov., was recently described from the Wombat maar lake fill (Grande et al., 2022), with at least one additional fish taxon awaiting detailed description.

As with the Giraffe maar sediments, there is ambiguity concerning the age of the Wombat

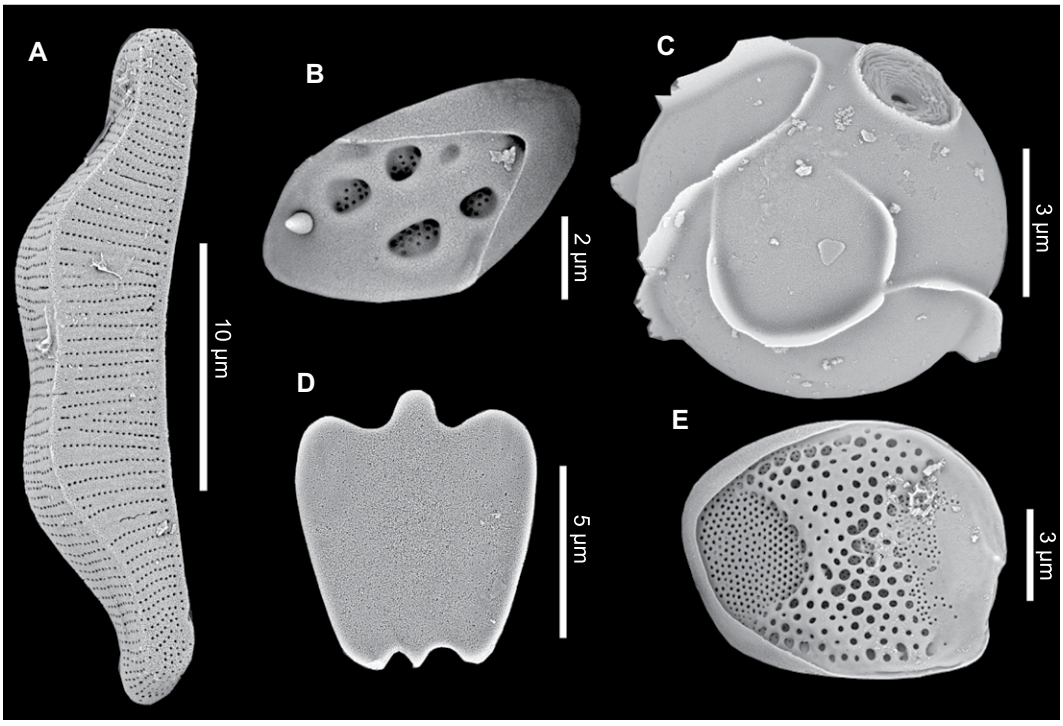

Figure 2. Siliceous microfossils uncovered in rocks from the Giraffe (A–C) and Wombat cores (D, E). (A) Valve of the diatom *Actinella goodwinii* Siver, Bishop, Wolfe and Lott; (B) synurophyte scale from the genus *Mallomonas* Perty; (C) chrysophyte cyst; (D) plate belonging to the testate euglyphid, *Scutiglypha* Foissner and Schiller; and (E) synurophyte scale from *Mallomonas schumachii* Siver.

maar. Unpublished phlogopite Rb-Sr model ages of ca. 2.5–1.8 Ga indicate contamination from local country rock or detrital sourcing (Siver et al., 2016). Siver et al. (2016), citing an abstract by Hu et al. (2011), suggested a Paleocene age for at least part of the Wombat lacustrine fill based on the absence of the Late Cretaceous pollen indicator taxa *Aquilapollenites* and *Wodehouseia*; the presence of *Ericaceiopollenites* and *Alnipollenites*; and the absence of *Platycarya*, an Eocene indicator taxon (Hu et al., 2011). However, there is no published radiometric age to substantiate biostratigraphic age inferences.

The aim of this study is to provide a revised geochronological framework for the Giraffe and Wombat maars using U-Pb zircon dating of distal rhyolitic tephra beds recovered from exploration drill cores that intersected the maar lake sediments. The dating techniques used were laser ablation–inductively coupled plasma–mass spectrometry (LA-ICP-MS) and chemical abrasion–isotope dilution–thermal ionization mass spectrometry (CA-ID-TIMS). To support this new geochronological framework for the Giraffe maar sediments, we present new glass fission-track results based on refined sample preparation methods and glass geochemistry of the tephra analyzed. We also present a revised, pollen-based biostratigraphic analysis for the Wombat maar sediment. Collectively, our results provide a robust geochronological underpinning for rare, high-latitude paleoenvironmental proxy records from early Cenozoic kimberlite maars.

2. GEOLOGICAL BACKGROUND

The Wombat (64.92°N, 110.45°W) and Giraffe (64.73°N, 109.75°W) kimberlite maars are situated in the Slave Craton within the Lac de Gras kimberlite field of the Northwest Territories, Canada (Fig. 1). The Slave Craton is an Archean granite-greenstone terrane of Neoarchean metaturbidites with syn- to post-tectonic granite, tonalite, and granodiorite plutons (ca. 2.63–2.58 Ga; Bowring and Williams, 1999; Nowicki et al., 2004). Studies of sedimentary xenoliths within kimberlite crater fills suggest that the region was covered by Middle Devonian strata and Cretaceous–Paleogene marine mudstones at various times (Nassichuk and McIntyre, 1996; Cookenboo et al., 1998; Sweet et al., 2003). Notably, xenoliths of Upper Cretaceous marine and Paleogene terrestrial sedimentary cover rocks, together with Paleogene post-eruptive maar sediments in the Lac de Gras kimberlite field, suggest that the transition from marine deposition in the Western Interior Seaway to deposition in isolated lacustrine settings occurred at some point during the Late Cretaceous (Sweet et al., 2003; Stasiuk et al., 2003, 2006; Ault et al., 2013).

Exploration drill cores BHP99-01 and BHP98-6 intersect the Giraffe diatreme. The kimberlite-rich, lowermost section of the BHP98-6 core is archived at Connecticut College (New London, Connecticut, USA), and the BHP99-01 core is archived at the Geological Survey of Canada (Calgary). Exploration drill core BHP99-01, collared at 47°, reveals ~80 VE m of undisturbed, organic-rich sedimentary fill comprising at least ~50 VE m of lacustrine sediment overlain by ~30 VE m of wood- and macrofossil-rich peat. The maximum thickness of the lacustrine facies is unknown because the base of the angled drill core intersected crystalline host rock. Detailed descriptions of the stratigraphy, sedimentology, and organic geochemistry of the Giraffe maar sedimentary fill were provided by Stasiuk et al. (2006) and Hamblin (2015).

Four tephra layers were recovered from drill core BHP99-01 and accessioned into the University of Alberta Tephrochronology Collection (Fig. 1; Table 1). The UA 1151/2842 (~5-cm-thick), 1152/2843 (~4-cm-thick), and 2845 (~4-cm-thick) tephra beds, which are stratigraphically just below the lacustrine-peat transition (Fig. 1), were light gray and finely laminated, with some rare plant detritus present. These samples are dominated by well-preserved platy, cuspate, and vesicular glass fragments. Due to stratigraphic proximity within 1.2 VE m of core, these samples were treated as a single sample, which is termed UA2842/3 henceforth. At 37.5 VE m below UA2842/3, tephra UA2844 (~10 cm thick) is stratigraphically the lowermost known tephra within the lacustrine section of the core. Tephra UA2844, which is brownish-gray and visibly more altered than the other samples, contains a mix of partially devitrified and well-preserved glass fragments.

TABLE 1. GIRAFFE AND WOMBAT TEPHRA SAMPLE IDENTIFICATION (ID) NUMBERS, CORE DEPTHS, THICKNESSES, AND WEIGHTS

Core ID	Tephra ID	Core depth (m)	Vertical equivalent depth (m)	Thickness (cm)	Sample weight (g)
Giraffe					
BHP99-01	UA2842	96.3	70.9	5	83.4
BHP99-02	UA2843	98.8	72.1	4	64.5
BHP99-03	UA2844	148.5	108.4	10	73.2
BHP99-04	UA2845	98.7	73.4	4	42.5
Wombat					
DDH00-5	UA3134	273.43	236.8	4	75.2
DDH00-5	UA3135	270.1	233.9	7	120.7

Note: Samples are stored in the collections of the University of Alberta Department of Earth and Atmospheric Science.

The Wombat kimberlite exploration efforts of BHP Billiton Diamonds, Inc., recovered three drill cores—CH93-29, DDH00-5, and DDH05-11 in 1993, 2000, and 2005, respectively. Most of the CH93-29 core is archived at Connecticut College, while DDH00-5 is housed at the Northwest Territories Geological Survey core archive in Yellowknife, Canada. A total of ~195 VE m of maar lake facies was intersected by CH93-29 and DDH00-5, which were drilled at angles of 45° and 60°, respectively. The upper ~180 VE m of the crater fill comprises dark, poorly consolidated, clay-rich laminites with rare lithic and country rock fragments. The lower ~15 VE m of the crater fill comprises gray laminated to massive siltstone with common flattened clay lenses, land plant detritus, and fully articulated fish fossil remains (Grande et al., 2022). Vivianite and siderite-goethite nodules are unevenly present throughout the lake facies, steadily increasing in abundance and size (up to 10 mm diameter) toward the top of the lacustrine sediments. Two tephra layers were found and sampled from each core at approximately the same correlated depth intervals near the bottom of the lacustrine succession, which indicates a potential region of stratigraphic overlap between the two cores (Fig. 1). Both tephra beds were light gray and finely laminated, with rare dark interlaminae. Zircon crystals for U-Pb dating were extracted from two tephra layers sampled from core DDH00-5 (Table 1; Buryak, 2020). Sample UA3134, ~4 cm thick, was dominated by well-preserved glass in the form of tricuspate and platy glass shards with rare, partially altered glassy-clay aggregates. The ~7-cm-thick UA3135 tephra, 2.9 m above UA3134, had a mix of partially altered glass pseudomorphs, glassy-clay aggregates, and unaltered glass shards with generally platy morphologies.

3. MATERIALS AND METHODS

3.1. U-Pb Zircon Geochronology

Zircon crystals were extracted from the tephra samples using conventional mineral separation methods of sieving, high-density liquid density separation, and microscopy. Individual zircon grains were handpicked under a stereoscopic microscope from the dense mineral fraction, mounted in epoxy, and lightly polished to remove adhered glass. Cathodoluminescence and backscattered-electron imaging of the zircon grains was done using a ZEISS EVO LS15 extended pressure–scanning electron microscope at the University of Alberta. Due to the small sample sizes (<120 g of tephra per sample) mandated by the small-diameter drill core (NQ, 47.6 mm core diameter), only a limited number of zircon crystals could be recovered.

3.1.1. Multicollector (MC)-ICP-MS

U-Pb analysis of individual zircon grains from the Wombat samples (UA3134 and UA3135) was performed on a New Wave Research 213 nm laser system coupled to a Nu Plasma I multicollector (MC)-ICP-MS at the Canadian Centre for Isotopic Microanalysis, University of Alberta. The analytical procedure was described in detail by Simonetti et al. (2005). Zircon crystals were spot ablated for 40 s using a 30 μm beam at a 5 Hz repetition rate and ~3 J/cm^2 laser energy at the sample surface. The primary reference material GJ-1 (608.5 ± 0.4 Ma; Jackson et al., 2004) and secondary zircon reference materials Plešovice (339.0 ± 2.6 Ma, this study; and 337.1 ± 0.4 Ma, Sláma et al., 2008) and 94-35 (55.7 ± 0.9 Ma, this study; and 55.5 ± 1.5 Ma, Klepeis et al., 1998) were analyzed before and after each set of 10–20 unknowns to monitor U-Pb fractionation, reproducibility, and instrumental drift. The ^{206}Pb-^{238}U ages generated for the secondary reference materials are within 2σ uncertainty of the literature values (Table S1[1]), while mean square of weighted deviate (MSWD) values for the entire suite of analyses are within the permissible range at the 95% confidence level for a single population of replicated analyses (Mahon, 1996). The ^{206}Pb/^{238}U average precision of these reference materials is ~2% (2σ) for individual spot analyses. All data were reduced offline using an in-house Microsoft Excel spreadsheet with unknowns normalized to the GJ-1 zircon primary reference standard. The uncertainties of measured isotopic ratios are a quadratic combination of the standard error of the measured isotopic ratio and the long-term excess scatter of the GJ-1 means. Common-Pb correction was applied using the ^{207}Pb method (Williams, 1997) with initial Pb composition (0.841) estimated from the Stacey and Kramers (1975) Pb-evolution model.

3.1.2. iCAP Quadrupole (Q)-ICP-MS

Zircon crystals from Giraffe samples UA2842 and UA2843 were analyzed at the Canadian Centre for Isotopic Microanalysis ICP-MS facility (University of Alberta) on a Thermo Scientific iCAP quadrupole (Q)-ICP-MS coupled to a New Wave Research UP-213 LA system. Zircon crystals were spot ablated for 40 s using a 30 μm beam at a 5 Hz repetition rate and ~3 J/cm^2 of laser energy at the sample surface. The primary reference material GJ-1 (605.5 ± 2.5 Ma; 608.5 ± 0.4 Ma; Jackson et al., 2004) and secondary zircon reference materials Plešovice (337.5 ± 2.7 Ma, this study; 337. ± 0.4 Ma, Sláma et al., 2008) and 94-35 (54.1 ± 1.3 Ma, this study; 55.5 ± 1.5 Ma, Klepeis et al., 1998) were analyzed before and after each set of 10–20 unknowns to monitor U-Pb fractionation, reproducibility, and instrumental drift. The ^{206}Pb-^{238}U ages for reference materials are within 2σ uncertainty of the established values (Table S2). MSWD values for the entire suite of analyses are within the permissible range at the 95% confidence level for the single population of replicated analyses (Mahon, 1996). The ^{206}Pb/^{238}U average precision of secondary reference materials is 1%–3% (2σ) for individual spot analyses. All data were processed using Iolite v3 (Paton et al., 2010, 2011) and the "VisualAge" data reduction scheme (Petrus and Kamber, 2012). For consistency, external uncertainties were propagated manually in an Excel spreadsheet in the same manner as the MC-ICP-MS data. Common-Pb correction was applied using the ^{207}Pb method (Williams, 1997) with initial Pb composition (0.838) estimated from the Stacey and Kramers (1975) Pb-evolution model.

3.1.3. CA-ID-TIMS

A subset of 10 Giraffe pipe zircon crystals from UA2842 and UA2843, and two zircon cyrstals from UA2844, were analyzed using CA-ID-TIMS at the Département des sciences

[1]Supplemental Material. LA-ICP-MS/CA-ID-TIMS U-Pb zircon data, tephra glass geochemistry, glass fission-track age data, and age modeling results. Please visit https://doi.org/10.1130/GSAB.S.25024565 to access the supplemental material, and contact editing@geosociety.org with any questions.

de la Terre, Université de Genève. The youngest crystals determined from the LA analysis of UA2842 and UA2843 were removed from the epoxy mounts for high-precision CA-ID-TIMS U-Pb dating. Due to extremely poor zircon recovery from the small sample of UA2844, only two zircon crystals were dated from this tephra. The extracted zircon crystals were first annealed in a muffle furnace at 950 °C for 48 h and then chemically abraded at 210 °C in concentrated hydrofluoric acid (HF) for 12 h following the approach of Widmann et al. (2019). After chemical abrasion, the zircon crystals were fluxed in 6N HCl overnight on a hot plate at 80 °C, and then cleaned ultrasonically and rinsed multiple times in 7N HNO_3. Following cleaning, crystals were loaded into individual Savillex microcapsules with ~70 µl of concentrated HF and ~5 mg of the EarthTime ET535 tracer solution (Condon et al., 2015). The microcapsules were then placed in a Teflon jacket and in a steel Parr digestion vessel, which was placed in the oven at 210 °C for 48 h for zircon dissolution. The dissolved samples were then dried on a hot plate at 80 °C, and three drops of 6N HCl were added to each to convert them to a chloride form, before they were returned to the Teflon jacket and Parr digestion vessel to be heated at 180 °C in the oven overnight. After the HCl conversion, the samples were loaded onto pre-cleaned anion exchange micro columns, and the U and Pb fractions were purified and collected in pre-cleaned Savillex beakers following a modified, eluant reduced version of the Krogh (1973) technique. After column chemistry, the samples were combined with silica gel and loaded onto outgassed, zone-refined Re filaments and placed in a Thermo Scientific Triton Plus MS for analysis following a method similar to that of Schaltegger et al. (2021). Pb isotopes were measured in dynamic mode on a MasCom secondary electron multiplier, while U isotopes were analyzed as UO_2 in static mode on Faraday cups with 10^{12} ohm resistors assuming an $^{18}O/^{16}O$ ratio of 0.00205. The mass-dependent isotopic fractionation for Pb was corrected using the long-term Pb fractionation values measured using a Pb double spike, which resulted in a Pb fractionation value of 0.15 ± 0.02 (%/amu). Uranium fractionation was controlled using the ET535 $^{233}U/^{235}U$ of 0.99506 and $^{238}U/^{235}U$ of 137.818 ± 0.045 (2σ; Hiess et al., 2012). U-Pb data reduction and uncertainty propagation were conducted using Tripoli and U-Pb ET-Redux software, both of which use the algorithms of McLean et al. (2011). All $^{206}Pb/^{238}U$ ages were corrected for initial Th disequilibrium assuming a partition coefficient relationship between the zircon Th/U and the magma Th/U of 0.2. All common Pb is assumed to be procedural blank and was corrected using the long-term lab blank isotopic composition of $^{206}Pb/^{204}Pb = 17.102 \pm 0.21$, $^{207}Pb/^{204}Pb = 15.40 \pm 0.11$, and $^{208}Pb/^{204}Pb = 36.17 \pm 0.25$ (all 1σ absolute). Data are summarized in Table S3.

3.2. Glass Fission-Track Dating

As initially reported by Westgate and Bray (2021), we used a slightly modified glass fission-track method to redate Giraffe tephra sample UT2115 from the University of Toronto tephrochronology collection; this sample was collected from the same tephra bed as UA2842 in core BHP99-01. We followed methods outlined in Wolfe et al. (2017) in all respects, with one exception: glass shards were etched with HF acid for an additional 15 s, thereby increasing total acid etch time from 180 s to 195 s. The glass fission-track age was calculated using the zeta-approach, based on the Moldavite tektite and its most current $^{40}Ar/^{39}Ar$ age of 14.808 ± 0.021 Ma (2σ; Schmieder et al., 2018). The Huckleberry Ridge tephra, with a $^{40}Ar/^{39}Ar$ sanidine age of 2.003 ± 0.014 Ma (Gansecki et al., 1998), was used as a secondary reference material for assessing the accuracy of the glass fission-track ages. The isothermal-plateau method was used to correct for partial track fading (Westgate, 1989). More detailed descriptions of glass fission-track age calculation are provided in Westgate (1989) and Sandhu and Westgate (1995). Glass fission-track data are summarized in Table S4.

3.3. Tephra Glass Geochemistry

Single-shard glass major element geochemistry was determined by wavelength-dispersive spectrometry on a JEOL 8900 or CAMECA SX100 electron microprobe at the University of Alberta using accelerating voltage of 15 keV, beam current of 6 nA, and beam diameter of 10 µm. Some analyses used a beam of 5 µm and the software Probe for EPMA (Donovan et al., 2015) to correct for any potential Na-loss using time-dependent intensity corrections (e.g., Jensen et al., 2021). Two secondary reference materials, Lipari obsidian (ID 3506) and Old Crow tephra glass (Kuehn et al., 2011), were run concurrently with all samples to assure proper calibration. All data were normalized to 100% on a water-free basis.

Trace element compositions were determined by LA-ICP-MS using a RESOlution ArF 193 nm excimer LA system coupled to a Thermo Scientific Element XR sector field (SF)-ICP-MS at the University of Alberta Arctic Resources Geochemistry Laboratory. Individual glass shards were analyzed with a beam of 10 µm or 23 µm in diameter at 2.8 J/cm^2 energy density (measured at the ablation site), with a 5 Hz repetition rate and 20 s of ablation time. ^{29}Si was used as an internal standard, and the instrument was calibrated against National Institute of Standards and Technology (NIST) SRM 612. NIST SRM 610, ATHO-G, and StHs 6/80-G were analyzed as secondary standards and reference materials to monitor accuracy and analytical reproducibility. All major/minor oxides, trace elements, and reference materials are listed in Tables S5 and S6.

3.4. Palynology

Six samples of the Wombat kimberlite maar sediments from cores DDH00-5 and CH93-95 were processed for palynological analyses following standard techniques (Traverse, 2007) at Global GeoLab Ltd., Medicine Hat, Alberta (Table 2). The samples were briefly subjected to hot treatments of HCl and HF and oxidation with Schulze's solution and stained with safranin O. Permanent mounts were made in liquid bioplastic. Microscopy was conducted using an Olympus BX61 transmitted light microscope at 400× and 1000× magnification under oil immersion. Quantitative analyses of palynomorphs were based on counts of unsieved preparations with mostly greater than 300 spores and pollen (median of 342, range of 206–556) from obligately terrestrial parent plants. The relative abundance of each taxon was based on this pollen sum. Non-terrestrial palynomorphs—including dinocysts, algae, acritarchs, and reworked palynomorphs—were also enumerated but excluded from the pollen and spore sum; their abundance is expressed as a proportion of the terrestrial pollen and spore sum. Palynological slides will be curated at the Northwest Territories Geological Survey.

TABLE 2. CORE SAMPLE IDENTIFICATION (ID) NUMBERS AND SAMPLING DEPTHS FOR THE WOMBAT MAAR LAKE SEDIMENTS USED FOR PALYNOLOGICAL ANALYSES

Core ID	Core sample ID	GSC number	Core depth (m)	Vertical equivalent depth (m)
DDH00-5	5-24-3-3	C-638543	194.1	168.1
DDH00-5	5-38-1-88	C-638544	262.7	227.5
DDH00-5	5-39-1-136_140	C-638545	267.9	232.1
DDH00-5	5-39-3-39	C-638546	270.1	233.9
DDH00-5	5-40-2-123_130	C-638547	273.7	237.0
CH93-29	93-29-67-4-64	C-638548	391.8	277.1

Note: GSC–Geological Survey of Canada.

4. RESULTS

4.1. U-Pb Zircon Age Calculations

Tephra depositional ages were calculated using the Bayesian modeling approach following Keller et al. (2018). Bayesian depositional age estimates were modeled assuming uniform, triangular distributions combined with a MELTS zircon crystallization model (Keller et al., 2018). The Bayesian model results we present are relatively insensitive to the choice of the prior. We prefer the triangular prior in each sample and report those ages in the following sections based on the following criteria: (1) since no closed-system zircon ages should postdate the eruption (except within analytical uncertainty), we expect a sharply truncated relative distribution of ages at the time of tephra deposition, and (2) the age distributions in each sample tend to take an approximately triangular form.

Additionally, we used IsoplotR v. 3.8 (Vermeesch, 2018) to calculate the maximum likelihood (Vermeesch, 2021) and the weighted mean of the youngest analyses that overlap at 2σ. These methods yielded depositional ages that are identical within a 95% confidence interval to those calculated using Bayesian modeling (Table S7). We prefer depositional ages based on the Bayesian modeling because this method decreases the impact of subjective interpretational decisions and is least likely to underestimate the reported uncertainty (e.g., Keller et al., 2018). All uncertainties are reported as absolute 2σ (95% confidence level). The CA-ID-TIMS depositional age uncertainties are shown as ± Y|Z, where Y is the measurement and spike calibration uncertainty and Z is the combined measurement, spike, and decay constant uncertainties.

4.1.1. Giraffe U-Pb and Glass Fission-Track Age

Most of the Giraffe tephra zircon grains were euhedral or partially broken fragments with a diameter size of between 40 μm and 120 μm. Additionally, zircon cathodoluminescence (CL) imaging shows simple internal structures with the majority of the crystals displaying oscillatory zoning or no visible zoning.

A total of 17 zircon crystals from sample UA2842 and nine grains from sample UA2843 were analyzed using iCAP-Q-ICP-MS (Fig. 3; Table S2). The Q-ICP-MS $^{206}Pb/^{238}U$ dates from this combined UA2842/UA2843 sample yielded a distribution of dates ranging from 50.5 Ma to 41.7 Ma. Ten grains from UA2842/UA2843 were dated using CA-ID-TIMS, yielding a tight range of $^{206}Pb/^{238}U$ dates ranging from 48.142 Ma to 48.02 Ma (Table S3). The best estimate for the depositional age was calculated using Bayesian modeling, yielding an age of 47.995 ± 0.082|0.087 Ma (Ypresian, Eocene) for the CA-ID-TIMS dates (Fig. 4). The revised isothermal plateau glass fission-track age of 54 ± 11 Ma (Lutetian–Thanetian; Eocene–Paleocene) (UT2115/UA2842; Table S6) is ~16 m.y. older than the previous estimate of 37.8 ± 4.0 Ma (Bartonian–Priabonian; Doria et al., 2011; Wolfe et al., 2017) and is consistent within uncertainty with the zircon U-Pb results (Fig. 4).

Only one of two dated zircon grains from sample UA2844 yielded a meaningful CA-ID-TIMS date of 48.72 ± 0.29|0.30 Ma (Ypresian). Although the date was based on only one dated grain, this estimate for the depositional age of UA2844 is ~700 k.y. older than the age of 47.995 ± 0.082|0.087 Ma obtained from the overlying UA2842/UA2843 tephra and is consistent with the stratigraphic position of the tephra samples.

4.1.2. Wombat U-Pb Age

From the Wombat kimberlite pipe, 34 zircon grains from tephra sample UA3135 and three zircon grains from tephra sample UA3134 were analyzed using MC-LA-ICP-MS. Most zircon grains were euhedral to subhedral, or partially broken fragments, with an average diameter of <60 μm. The CL imaging in both samples shows that oscillatory zoning is the predominant type of internal texture, though some grains exhibit no visible zoning. Several grains from sample UA3135 had glass rims, which suggests that they interacted with melt during the eruption. The common Pb-corrected $^{206}Pb/^{238}U$ dates from sample UA3134 were not coherent. Two zircon grains gave ages of ca. 190 Ma, and one grain was dated at ca. 1370 Ma. These new ages are not consistent with the known timing of kimberlite magmatism on the Slave craton (Creaser et al., 2004; Sarkar et al., 2015), suggesting contamination by xenocrysts or detrital material during the eruption from volcanic and/or crustal sources.

In contrast, common Pb-corrected $^{206}Pb/^{238}U$ dates from sample UA3135 yielded a tighter age range from 99.1 Ma to 72.9 Ma. The Bayesian model gave a $^{206}Pb/^{238}U$ age of 80.9 ± 1.0 Ma (Campanian; Figs. 5A and 5B). One zircon grain produced an age of 72.9 ± 1.5 Ma (39-3-39-12; Table S1), which is much younger than the main population, and thus it was considered an outlier and excluded from the age calculation. We interpret this young apparent age as the result of radiogenic Pb loss from the zircon supported by the decrease in measured $^{206}Pb/^{238}U$ as a function of increasing depth/time during ablation (Fig. S4). Normally, the opposite Pb/U laser-induced fractionation trend is observed during U-Pb zircon analysis. Thus, we prefer the Bayesian model age of 80.9 ± 1.0 Ma and report it henceforth.

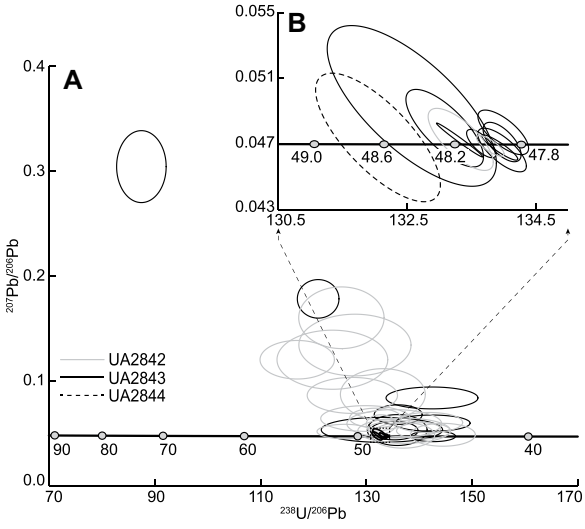

Figure 3. (A) Concordia diagram of all Giraffe tephra zircon U-Pb analyses. (B) Enlarged inset of chemical abrasion–isotope dilution–thermal ionization mass spectrometry zircon analyses only, marked by dashed box in part A.

4.2. Tephra Glass Characterization and Geochemistry

4.2.1. Giraffe Results

Glass shards from all Giraffe tephra samples (UA1151/2842, UA1152/2843, UA2844, and UA2845) are relatively homogenous high-silica rhyolites ranging from ~76.5 wt% to 77.6 wt% (Fig. 6). The Na_2O and K_2O wt% values suggest that much of the glass is at least minimally altered, with evidence for Na-loss and K-enrichment (and loss in more extreme cases), occasionally leading to overly high SiO_2 values (>78 wt%). However, despite this, each sample contains a proportion of glass that remains geochemically coherent, including oxides such as MgO and CaO that may become highly variable with increased weathering (e.g., Fisher and

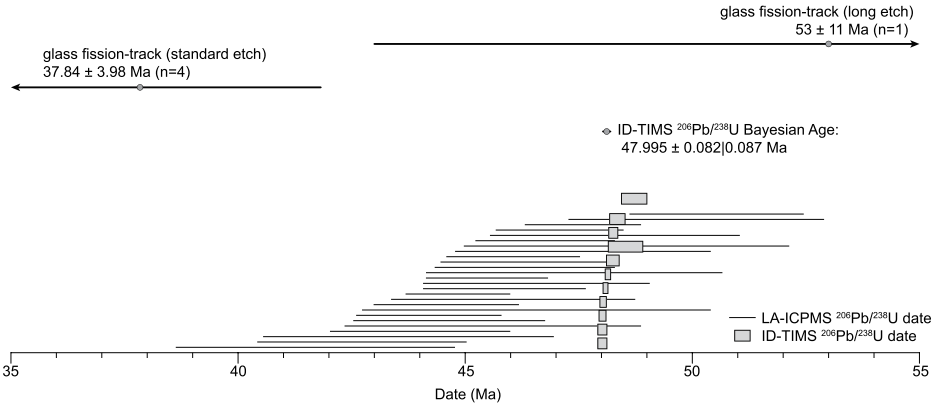

Figure 4. $^{206}Pb/^{238}U$ chemical abrasion–isotope dilution–thermal ionization mass spectrometry (CA-ID-TIMS) and laser ablation–inductively coupled plasma–mass spectrometry (LA-ICP-MS) point ages and Bayesian modeling results for Giraffe tephra zircon and comparison of glass fission-track ages of samples UT2115/UA2843 using increased hydrofluoric acid (HF) etch time.

Schmincke, 1984; Jensen et al., 2021; Table S5). When the most egregiously weathered glass analyses are removed, all four tephra beds share some similarities, including higher alkali contents ($K_2O + Na_2O = \sim$7–8 wt%) and lower CaO wt% (~0.85–0.25 wt%), with samples UA1151/2842 and UA1152/2843 being virtually identical (Fig. 7). Samples UA2844 and UA2845 are distinguished based on Al_2O_3, FeOt, and CaO wt%, with UA2844 having low FeOt (~0.50 wt%) and UA2845 having very low CaO (~0.25 wt%; Fig. 7; Table S5).

Chondrite-normalized rare earth element patterns of glass from samples UA1151/2842 and UA1152/2843 show only subtle differences between the two samples (Fig. 8; Table S6). Specifically, light rare earth element (LREE) patterns overlap, and both are enriched in heavy rare earth elements (HREEs; UA2842 $La_N/Yb_N = 7.7$; UA2843 $La_N/Yb_N = 8.3$), with a distinct negative europium anomaly (UA 2842 $Eu/Eu^*_N = 0.46$; UA2843 $Eu/Eu^*_N = 0.45$). In contrast, the glass composition from sample UA2845 displays higher trace element abundances, except for Sr, Cs, and Ba, which are depleted. Overall the glass rare earth element (REE) pattern of sample UA2845 shows LREE enrichment in the REE ratio ($La_N/Yb_N = 4.7$) with a negative europium anomaly, $Eu/Eu^*_N = 0.36$. Trace element glass data from sample UA2844 is inconclusive since only a limited number of analyses could be performed due to the small size of glass fragments and devitrification. However, initial data suggest a trace element pattern more comparable to those of samples UA1151/2842 and UA1152/2843 (Table S6).

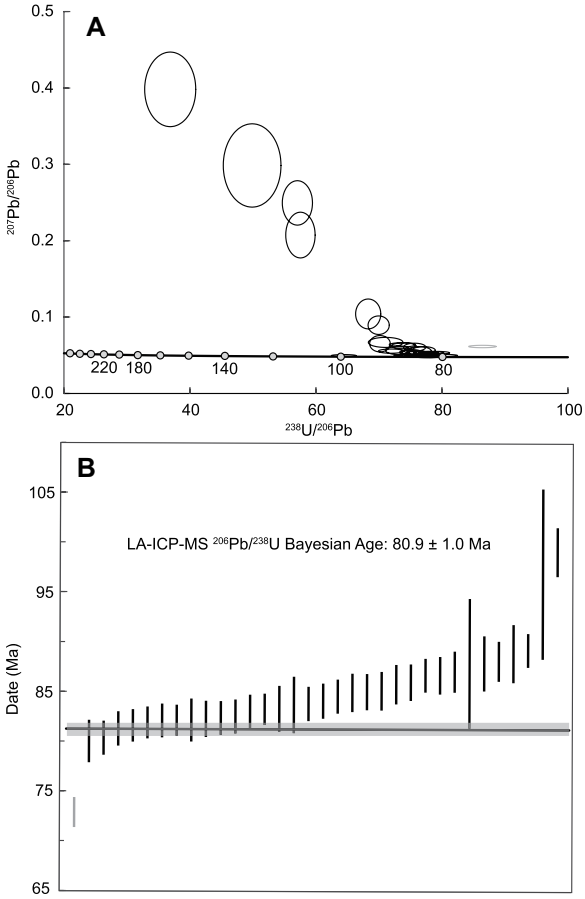

Figure 5. (A) Concordia plot of all Wombat zircon laser ablation–inductively coupled plasma–mass spectrometry (LA-ICP-MS) U-Pb analyses. (B) Bayesian model $^{206}Pb/^{238}U$ age for the UA3135 tephra layer.

4.2.2. Wombat Results

Glass samples from Wombat tephra are also rhyolites but with lower SiO_2 wt% compositions than the Giraffe tephra, ranging between ~73 wt% and 74 wt% (Fig. 6). The glass major/minor element analyses of sample UA3134 contain a surprisingly unweathered population of glass (given its age) that may be a good representation of its original composition (Fig. 7; Table S5). In contrast, sample UA3135 contains fewer intact glass shards, and all analyses have distinctly low Na_2O wt% (~<1.8 wt%), which is indicative of alteration. Interestingly, the other oxides remain relatively homogenous and are not dissimilar to UA3134, but only notably different in Al_2O_3 wt%.

No significant variability is observed in the range of trace element concentrations despite the weathered conditions of many shards in these two samples. Sample UA3134 has average values (±1SD) of 56.3 ± 2.7 ppm Rb, 187.9 ± 5.5 ppm Sr, 37.0 ± 1.6 ppm Y, 209.9 ± 4.5 ppm Zr, 5.5 ± 1.0 ppm Nb, 951.4 ± 24.8 ppm Ba, and 14.2 ± 0.7 ppm La. The LREE are enriched relative to HREE, with $La_N/Yb_N = 2.7 \pm 0.7$, and there is a negative europium anomaly ($Eu/Eu^*_N = 0.58$) (Fig. 8; Table S6). Sample UA3135 has average values (±1SD) of 95.0 ± 5.2 ppm Rb, 109.2 ± 2.2 ppm Sr, 23.0 ± 0.9 ppm Y, 126.7 ± 5.2 ppm Zr, 3.8 ± 0.4 ppm Nb, 1041.8 ± 36.4 ppm Ba, and 14.8 ± 0.5 ppm La (Table S6). The sample UA3135 glass LREEs are slightly more enriched ($La_N/Yb_N = 3.9 \pm 0.3$), with a more distinct negative Eu anomaly ($Eu/Eu^*_N = 0.77$) than that of sample UA3134 (Fig. 8; Table S6).

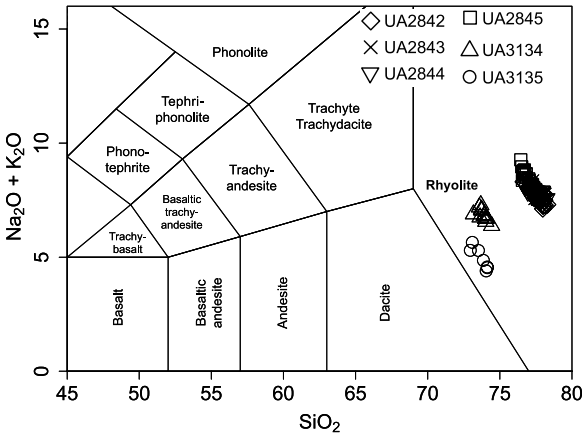

Figure 6. Total alkali-versus-silica plot, after LeBas et al. (1986), for the Wombat and Giraffe tephra glass analyses.

4.3. Palynology

Recovery from the six palynological samples ranged from poor to good, and preservation of palynomorphs ranged from fair to exceptional (Fig. 9). All samples yielded a thermal alternation index of 0 (Staplin, 1969; Pearson, 1984). Complete details of pollen results are provided in Galloway et al. (2022).

The uppermost five samples (C-638543 through C-638547, spanning 168.1–237.0 VE m core depth, Table 2) have broadly similar pollen assemblages. Cupressaceae-Taxacaeae (49%–70%) and *Pinuspollenites* (11%–21%) dominate the pollen assemblages (Fig. 10). *Caryapollenites* is a dominant angiosperm pollen, representing 2%–5% of the assemblages. *Metasequoia* and *Cycadopites* pollen are commonly present, at proportions of 3%–8% and 2%–5%, respectively. *Equisetum*, *Quercoidites*, and *Betulaceoipollenites* pollen are also present at low abundances (<5%; Fig. 10). Spores are rare to absent, and dinocysts are absent. In this suite of samples, C-638546 (233.9 VE depth) is notable because it was collected from the same tephra bed that was dated by zircon U-Pb methods.

The stratigraphically lowest sample (C-638548, 277.1 VE m depth) yielded an assemblage that is distinct from the other preparations. Cupressaceae-Taxaceae pollen (18%) is less abundant than in the other preparations, although *Pinuspollenites* (11%) and *Cycadopites* (4%) pollen are similar in abundance to samples from younger strata in the lacustrine successions, and *Caryapollenites* (4%) and *Bet-*

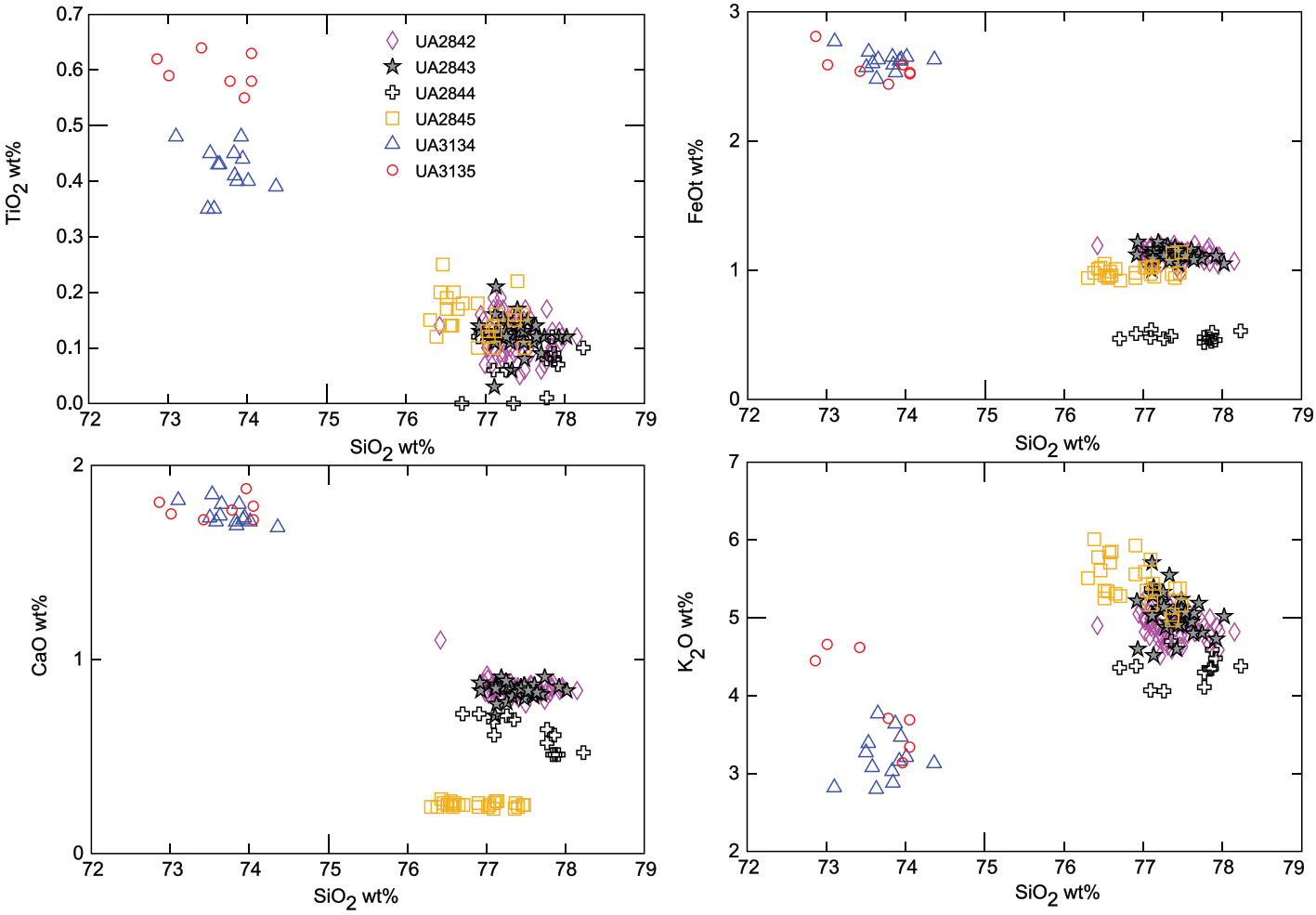

Figure 7. Bivariate plots detailing the major and minor element compositions of the Wombat and Giraffe maar sediment tephra glass samples.

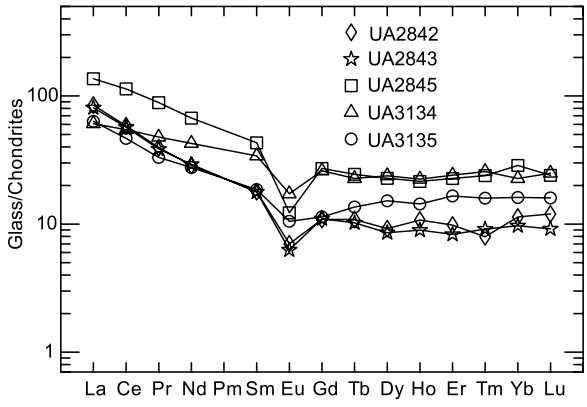

Figure 8. Chondrite-normalized (Sun and McDonough, 1989) rare earth element spider diagram for laser ablation–inductively coupled plasma–mass spectrometry results from Giraffe and Wombat maar sediment tephra glass.

ulaceoipollenites (3%) pollen are similar. Pollen taxa unique to this sample include *Perinopollenites elatoides* (5%), *Laricoidites magnus* (4%), and *Rugubivesiculites*. The proportion of spores and their diversity is highest in this sample and includes *Baculatisporites comaumensis* (6%), *Deltoidospora hallei* (5%), *Osmundacidites wellmannii* (3%), and *Laevigatosporites ovatus* (2%) (Fig. 10). Notable absences from all of the Wombat palynology samples are the Eocene indicator taxon *Platycarya* (see Hu et al., 2011) and *Aquilapollenities*, and *Wodehousiea*, which are common in the Late Cretaceous in western North America (see discussion in Galloway et al., 2022).

The basal sample contains abundant and diverse (30%) dinocysts with 31 cyst taxa identified across 22 genera, including 22 taxa identified at the species level (M. Bringué *in* Galloway et al., 2022). Notable dinocyst taxa in this sample include *Alterbidinium acutulum*, *Isabelidinium cooksoniae*, *Trithyrodinium rhomboideum*, and *Trithyrodinium singhii*, and taxa with important biostratigraphic significance, such as *Bourkidinium psilatum*, *Dorocysta litotes*, *Florentinia verdieri*, *Luxadinium propatulum*, *Pervosphaeridium cf. cenomaniense*, *Tanyosphaeridium* sp. C (Brideaux and McIntyre, 1975), *Tenua scabrosa*, and *Wallodinium luna* (M. Bringué *in* Galloway et al., 2022).

5. DISCUSSION

5.1. Timing of the Giraffe Maar Sedimentation and Its Implications

5.1.1. The Giraffe Maar Zircon U-Pb Age

The CA-ID-TIMS zircon U-Pb dates provide the most accurate and precise constraints on the timing of Giraffe maar sedimentation. The sample UA2842/3 Bayesian age of 47.995 ± 0.082|0.087 Ma provides a precise chronological marker for the uppermost section of the lacustrine sediments in the drill core, and the transition to peat deposition in the maar basin. The sample UA2844 single-grain $^{206}Pb/^{238}U$ age of 48.72 ± 0.29|0.30 Ma provides the first direct geochronological data for the lower section of the lacustrine strata, which enables construction of a simple, preliminary age-depth model for future paleoenvironmental proxy analyses of the ~50-m-thick lacustrine succession. This single grain age could represent one or more earlier stages of zircon growth predating the timing of eruption and tephra deposition (i.e., antecryst), and is best interpreted as a maximum age estimate for the deposition of this tephra horizon. The individual LA U-Pb zircon ages from sample UA2842/3 are younger (up to ~8%) than the CA-ID-TIMS result and the Rb-Sr phlogopite kimberlite emplacement age from the same samples. This apparent age offset is likely due to minor lead loss associated with damage to zircon crystal lattice as a result of U decay and potentially more errors associated with primary reference materials that are much older than the samples. The zircon crystals analyzed by TIMS were chemically abraded prior to analysis to remove the effects of Pb loss and therefore produced older—and likely more accurate—ages (Widmann et al., 2019). The CA-ID-TIMS results overlap with the diatreme Rb-Sr emplacement age of 47.8 ± 1.4 Ma, and also the revised sample UA2842 glass fission-track age of 53 ± 11 Ma. Though the substantially lower precision of the Rb-Sr and glass fission-track ages makes it difficult to infer details of maar sedimentation, the overlap within dating uncertainty between Rb-Sr–dated kimberlite emplacement and the CA-ID-TIMS age for tephra deposition at the lacustrine/peat transition suggests that the maar lake formed directly after eruption.

A major implication of our tephra zircon U-Pb dating is the ~10 m.y. difference between the ca. 48 Ma ages reported here and the 37.8 ± 4.0 Ma glass fission-track age for the same tephra, as reported by Doria et al. (2011) and Wolfe et al. (2017). The only difference in sample treatment was an additional 15 s of HF acid etching for the ca. 48 Ma age reported here, which suggests that longer etch times are required for glass fission-track analyses of early Cenozoic glasses (e.g., Westgate and Bray, 2021). The annealing temperature for glass is low, leading to fission-track fading even under ambient surface temperatures. Thus, it is likely that the original HF etch time applied in Doria et al. (2011) and Wolfe et al. (2017) was insufficient to reveal all of the annealed fission tracks, leading to lower measured spontaneous track density and, in turn, a younger calculated fission-track age. Under-etching is also a known concern for fission-track dating of young zircon (e.g., Kohn et al., 1992; Seward and Kohn, 1997), and we demonstrate here that under-etching can also yield substantial inaccuracy when dating older glasses.

5.1.2. Giraffe Maar Tephra Geochemistry and Potential Source Regions

The location of the source volcano(s) that produced the Giraffe tephra deposits is not known. Glass shards from samples UA 1151/2842 and UA1152/2843 have similar trace and major element compositions and are enriched in Ba (1300–1600 ppm). UA2845 is very different from the other samples, including those from Wombat, with lower Ba (~225 ppm), very depleted Sr (~2.5 ppm), and enriched concentrations of Nb and all LREEs except Eu. Sample UA2844 has too few trace element analyses for any firm conclusions, but the major and trace element data suggest it is more like the upper Giraffe tephra than sample UA2845. Using the tectonic discrimination diagrams of Schandl and Gorton (2002), glass data for all of the tephra samples broadly plot in the active continental margin field or the margin with oceanic arc fields (Fig. 11). Classifications on these discrimination diagrams can be misleading as they are based on whole-rock analyses; however, comparing these data to those available in the literature for tephra glasses shows them to be within the compositional range of typical arc volcanics. The one partial outlier is sample UA2845, with its exceptionally depleted Sr, low Ba, very low CaO wt%, and high K_2O wt%. This geochemical pattern was observed in numerous Neogene volcanic glasses from intraplate volcanic regions including (but not limited to) various centers around the Long Valley Caldera, such as Glass Mountain and the Mono-Inyo craters in California, USA, South Mountain Rhyolite of the Valles Caldera, New Mexico, USA, and the High Rock Caldera complex of Nevada, USA (e.g., Noble et al., 1972, 1979; Ren et al., 2003; Coble and Mahood, 2016; Jensen et al., 2021). There are also some examples of compositionally similar tephra from arc-related

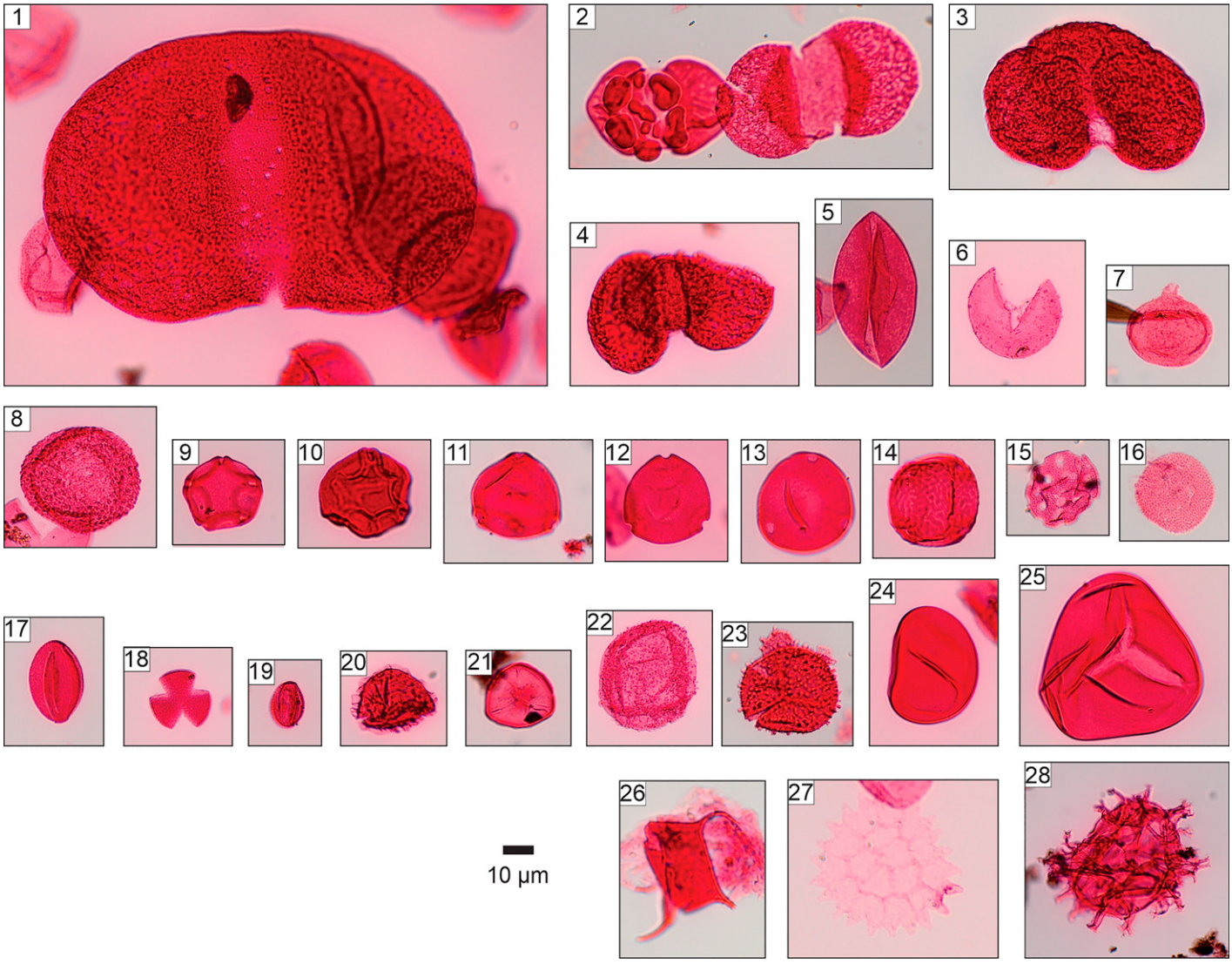

Figure 9. Photographs of selected pollen, spores, and non-pollen palynomorphs preserved in preparations of samples from drill cores CH93-29 and DDH00-5. Microscopy conducted with an Olympus BX-53 transmitted light microscope at 400× magnification under oil immersion. Photos were captured using an Olympus SC50 camera and Olympus cellSens imaging software. Some specimens were photographed during post-enumeration scanning and are therefore not necessarily represented in Figure 8. Information for samples detailed below include taxon name, taxonomical authority where applicable, sample, depth (m, vertical equivalent, VE), run number ("R" number), GSC Curation number ("C"-number), and England Finder coordinates. See Galloway et al. (2022) for full details on palynological analyses. (1) *Piceapollenites* sp., sample 5-40-2-123_30, 237.0 VE m, R3830-5, C-638547, X27/2; (2) *Rugubivesiculites* cf. *R. multisaccus* Singh 1983 (left) and undifferentiated bisaccate pollen (right), sample 5-38-1-88, 227.5 VE m, R3830-2, C-638544, S27/3; (3) undifferentiated bisaccate pollen, sample 5-40-2-123_130, 237.0 VE m, R3830-5, C-638547, Y29/1; (4) Podocarpaceae sample 5-39-1-136_140, 232.1 VE m, R3830-3, C-638545, S36-2; (5) *Cycadopites follicularis* Wilson and Webster 1946, sample 5-40-2-123_130, 237.0 VE m, R3830-5, C-638547, W27/3; (6) Cupressaceae-Taxaceae, sample 5-39-1-136_140, 232.1 VE m, R3830-3, C-638545, T35/2; (7) *Metasequoia* sp., sample 5-38-1-88, 227.5 VE m, R3830-2, C-638544, X26/2; (8) *Cerebropollenites mesozoicus* (Couper 1958) Nilsson 1958, sample 5-40-2-123_130, 237.0 VE m, R3830-5, C-638547, O17/1; (9) *Alnipollenites* sp., sample 5-24-3-3, 168.1 VE m, R3830-1, C-638543, Q29/4; (10) *Paraalnipollenites alterniporus* (Simpson) Srivastava 1978, sample 5-39-1-136_140, 232.1 VE m, R3830-3, C-638545, U35/4; (11) *Coryluspollenites* sp., sample 93-29-67-4-64, 277.1 VE m, R3830-6, C-638548, N26/1; (12) *Momipites* sp., sample 5-40-2-123_130, 237.0 VE m, R3830-5, C-638547, S41/4; (13) *Caryapollenites* sp., sample 5-40-2-123_130 R3830-5, C-638547, S28/3; (14) *Ulmipollenites* sp., sample 5-40-2-123_130, 237.0 VE m, R3830-5, C-638547, Q29/3; (15) *Cretacaeiporites* sp., sample 93-29-67-4-64, 277.1 VE m, R3830-6, C-638548, R23/3; (16) *Liliacidites* sp., sample 5-38-1-88, 227.5 VE m, R3830-2, C-638548, X27/2; (17) *Quercoidites* sp., sample 5-40-2-123_130, 237.0 VE m, R3830-5, C-638547, Y29/1; (18) *Retricolpites* sp., sample 5-40-2-123_130, 237.0 VE m, R3830-5, C-638547, U38/4; (19) *Salixpollenites* sp., sample 5-24-3-3, 168.1 VE m, R3830-1, C-638543, Q29/4; (20) *Retitriletes austroclavatidites* (Cookson 1953) Döring et al. in Krutzsch 1963, sample 5-39-3-39, 233.9 VE m, R3830-3, C-638546, X21/2; (21) *Stereisporites antiquasporites* Dettmann 1963, sample 93-29-67-4-64, 277.1 VE m, R3830-6, C-638548, R39/3; (22) *Osmundacidites wellmannii* Couper 1953, sample 5-39-3-39, 233.9 VE m, R3830-4 C-638546, W37/2; (23) *Baculatisporites comaumensis* Potonié

1953, sample 5-38-1-88, 277.5 VE m, R3830-2, C-638544, S36/2; (24) *Laevigatosporites ovatus* Wilson and Webster 1946, sample 5-39-3-39, 233.9 VE m, R3830-4, C-638546 (tephra horizon), P17/2; (25) *Cyathidites australis* Couper 1953, sample 5-39-3-39, 233.9 VE m, R3830-4, C-638546 (tephra horizon), Z39/2; (26) unidentified acritarch, sample 93-29-67-4-64, 277.1 m VE, R3830-6, C-638548, no England Finder coordinates; (27) *Pediastrum* Meyen 1829, sample 5-40-2-123_130, 237.0 m VE, R3830-5, C-638547, S26/2; (28) unidentified dinoflagellate cyst, sample 93-29-67-4-64, 277.1 m VE, R3830-6, C-638548, V32/4.

volcanoes, such as Uzon Caldera and Bolshoi Semiachik, Kamchatka (Portnyagin et al., 2020), and several tephras associated with calderas in Central America, although these tend to have higher BaO (e.g., Mixta Pumice, Guatemala; e.g., Schindlbeck et al., 2018). This does raise the possibility that some of these tephra may be intercontinental rather than arc-related. Also notable is that this geochemical signature appears to be strongly associated with calderas.

Recently, Westgate and Bray (2021) proposed that the most likely candidate for the source of the UA2842/43 Giraffe tephra could be located ~1500 km west of Lac de Gras in east-central Alaska, USA, where a thick pile of Paleocene (57.8 ± 1.7 Ma; K-Ar) rhyolitic-welded ignimbrites was found (site EC; Bacon et al., 1990). This tentative source attribution was based on the distinctive high Ba concentration in sample UA2842/43 and other volcanic rocks in the proposed source area. However, there are no known chemical analyses for the 57.8 Ma welded ignimbrites, and their existing K-Ar geochronology is inconsistent with the younger U-Pb ages reported here for the Giraffe tephra.

5.1.3. Timing of the Giraffe Maar Lake Sedimentation

Previously, based on palynological examination of xenoliths from volcaniclastics in the Hardy Lake kimberlites, Scott Smith and McKinlay (2002) and Scott Smith (2008) suggested that some kimberlite post-eruptive craters in the Lac de Gras field could have infilled slowly following a long period (possibly millions of years) of no sedimentation. In contrast, Moss et al. (2008) suggested rapid onset of sedimentation in the post-eruption crater, based on examination of crater-facies deposits and pipe geometry of the A154N kimberlite pipe.

The U-Pb date of 48.72 ± 0.29|0.30 Ma for the lower lacustrine facies in the Giraffe maar, in conjunction with the Rb-Sr age of 47.8 ± 1.4 Ma for kimberlite emplacement (Creaser et al., 2004), suggest that water infilled the post-eruptive crater nearly instantaneously. Assuming this single zircon age accurately constrains the timing of initial lacustrine sedimentation, the U-Pb age of 47.995 ± 0.082|0.087 Ma from the upper section of the lake succession indicates that the lake infilled with sediment relatively slowly over ~700 k.y., at a sedimentation rate of ~0.06 ± 0.04 mm/yr). This estimate for the duration and rate of lacustrine sedimentation is hampered by the low precision of the U-Pb date for the lower tephra (UA2845) and the lack of intermediate dated horizons to corroborate the core age-depth model. Nevertheless, the data suggest that Lac de Gras maar lakes were relatively short-lived water bodies with sedimentation beginning directly after kimberlite emplacement, which is consistent with the assessment of Moss et al. (2008). Slow sedimentation rates of ~0.1 mm/yr for the Giraffe maar are broadly consistent with the sedimentation rate estimates from other maar lake localities, including the Eocene Eckfeld maar (~0.4 mm/yr; Mingram, 1998) and Messel maar (~0.15 mm/yr; Lenz et al., 2015). This sedimentation rate is also consistent with Holocene sedimentation rates of lakes on the Canadian Shield in the Northwest Territories (Crann et al., 2015) but is lower than mean sedimentation rates of lakes in mid-latitude (1.0 mm/yr) and southeastern (2.2 mm/yr) North America over the past 150 years (Brothers et al., 2008).

5.1.4. Implications for Early Eocene CO_2 Reconstruction and Paleoclimate

The early Eocene was marked by short-lived hyperthermal events that culminated in the Early Eocene Climatic Optimum (EECO), which was a sustained hyperthermal interval with a global mean surface temperature that was ~13 °C warmer than at present (Inglis et al., 2020). Cooling that began in the middle Eocene (e.g., Zachos et al., 2008) marks the terminal interval of the Paleogene greenhouse world, with the onset of ice-sheet glaciation on Antarctica by the earliest Oligocene (e.g., Pagani et al., 2011).

Previous multi-proxy paleoclimatic reconstructions from the Giraffe maar lacustrine sediments and peat indicate that the region supported

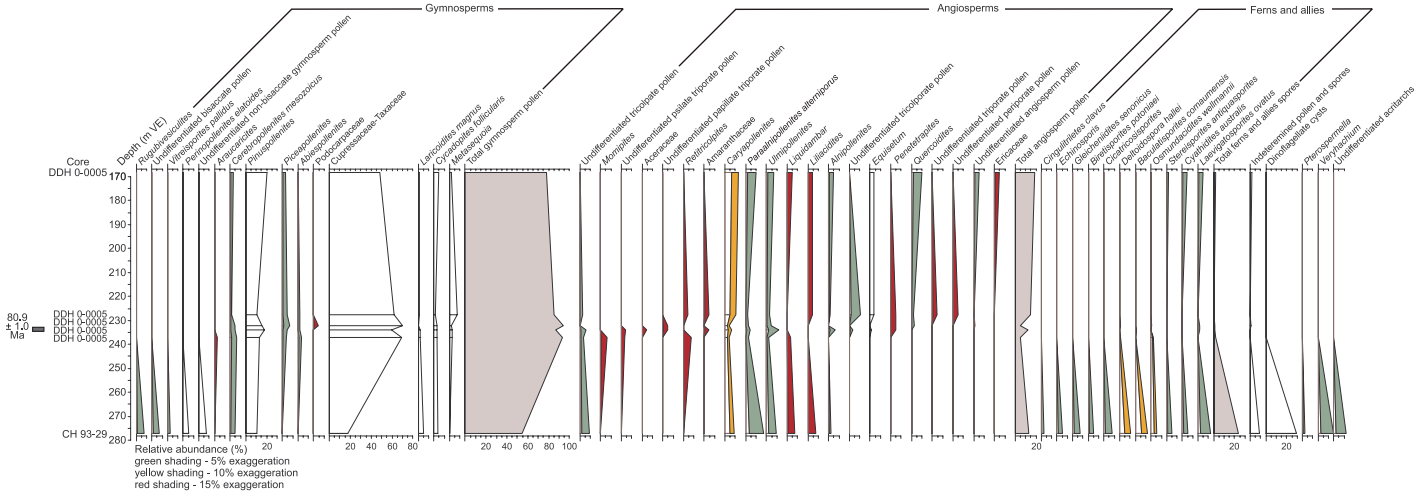

Figure 10. Stratigraphic diagram showing the relative abundance of pollen, spores, and non-pollen palynomorphs enumerated in preparations of samples from drill cores CH93-29 and DDH00-5 of the Wombat kimberlite, Northwest Territories, Canada. Plotted using TiliaGraph (Grimm, 1993). VE—vertical equivalent.

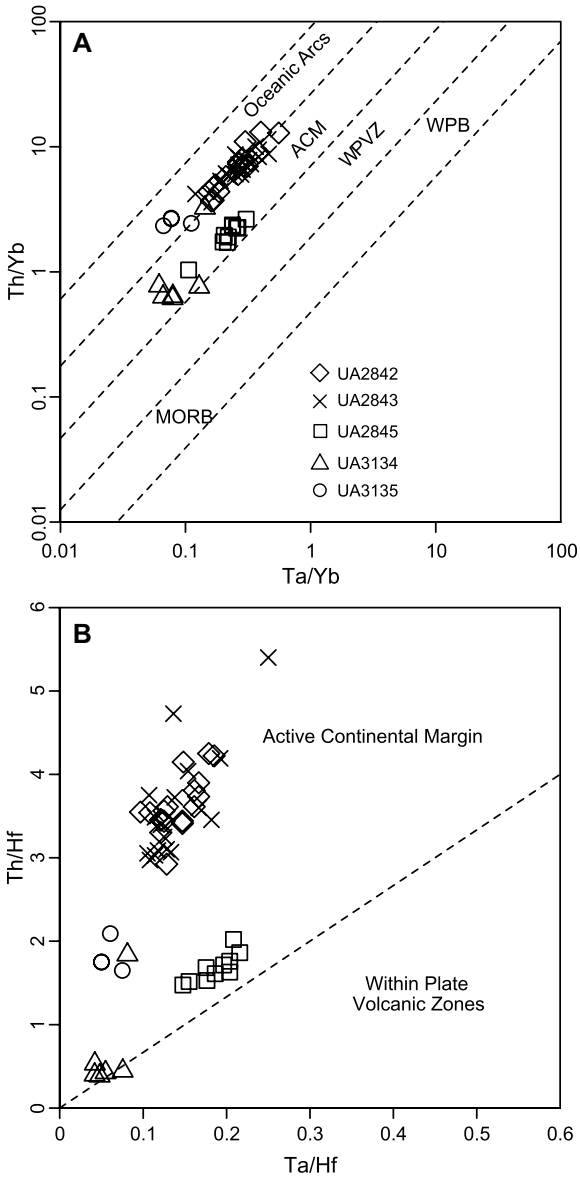

Figure 11. Tectonic discrimination diagrams after Schandl and Gorton (2002), showing the Wombat and Giraffe maar sediment tephra glass that plots in the active continental margin (ACM) field or on the margin with oceanic arc field. WPVZ—within-plate volcanic zone; MORB—mid-oceanic-ridge basalt; WPB—within-plate basalt.

a humid-temperate forest ecosystem under only modestly higher-than-present radiative forcing from atmospheric CO_2 (Wolfe et al., 2017). Wolfe et al. (2017) used a previous glass fission-track age of 37.8 ± 4.0 Ma (Doria et al., 2011) to propose a latest middle Eocene age for the fossil-bearing horizons that conformably overlie the maar lake sediments, which showed that the Canadian subarctic was ~17 °C warmer (mean annual temperature) and about four times wetter (mean annual precipitation) than at present. Stomatal index and gas-exchange model studies of *Metasequoia* foliage, from the same sediments used to reconstruct paleoclimate, yielded a mean reconstructed atmospheric CO_2 concentration of ~490 ppm (380–780 ppm at 1σ; Doria et al., 2011; Wolfe et al., 2017). This estimate of atmospheric CO_2 concentration is likely an underestimate by <100 ppm, based on a forthcoming revision of the gas-exchange modeling from new carbon isotopic and stomatal geometry measurements of *Metasequoia* foliage using methodological improvements following Liang et al. (2022).

The revised ca. 48 Ma age (Ypresian, early Eocene) of the Giraffe maar sediments places this record at a time of higher atmospheric CO_2 concentration. Although there is substantial variability in the current estimate of atmospheric CO_2 during the latter part of the early Eocene at ca. 48 Ma (e.g., Anagnostou et al., 2020; Wong et al., 2021; Ring et al., 2022), the stomata-based CO_2 reconstruction from the Giraffe maar fill remains on the low end of the range of proxy estimates. The pollen-based mean annual temperature of 14.5 ± 2.6 °C for the Giraffe site (2σ; Wolfe et al., 2017) is consistent with available terrestrial paleoclimatic reconstructions (within dating uncertainty) of ca. 48 Ma from the northern high latitudes (e.g., Eldrett et al., 2009; Greenwood et al., 2010; Suan et al., 2017). The Giraffe record thus provides an important proxy constraint for model-data comparisons of greenhouse paleoclimate, such as recent simulations with an improved ability to simulate the extreme high-latitude warming under CO_2 conditions that are more consistent with available proxy data (e.g., Zhu et al., 2019).

The pollen assemblage reported by Wolfe et al. (2017) preserved in the Giraffe kimberlite pipe is broadly similar to the composition of assemblages preserved in the upper five samples of the Wombat kimberlite pipe, in particular that Cupressaceae dominates the gymnosperm pollen, and fagalean types (*Quercoidites* and *Corylus*) are important angiosperm elements. Notable differences are that Wolfe et al. (2017) reported the presence of the Eocene indicator *Platycarya swasticoides* pollen, and in the Giraffe material, angiosperm pollen are more abundant than gymnosperm pollen (53%–74% of the assemblage). In the Wombat material, gymnosperm pollen ranges from 78% to 94% of the assemblage, angiosperm pollen comprises only 5%–19% of the assemblage, and spores from ferns and allies comprise between <1% and 2% of the assemblage. The basal sample (C-638548) is distinct in that the preparation contains 54% gymnosperm pollen, 13% angiosperm pollen, and 24% of taxa with affinities to ferns and allies.

5.2. Timing of the Wombat Maar Sedimentation and Its Implications

5.2.1. The Wombat Maar Zircon U-Pb Age

We interpret the UA3135 zircon U-Pb weighted mean age of 80.9 ± 1.0 Ma (Campanian) to be the best maximum age estimate for the onset of Wombat maar lacustrine sedimentation. On this basis, we place the start of the lake infilling around the early Campanian during the Late Cretaceous (following Gale et al., 2020). The Wombat kimberlite does not have an established emplacement age, with previous attempts using phlogopite Rb-Sr model ages (R. Creaser, 2016, personal commun., cited in Siver et al., 2016) and U-Pb rutile (C. Sarkar, 2019, personal commun.) that yielded inconclusive data. However, a spatially broad comparison of the Wombat tephra zircon ages with the known radiometric emplacement ages from the Lac de Gras and Hardy Lake kimberlite fields shows that there is a consistent temporal correlation. The oldest Cretaceous kimberlites with known emplacement ages (Heaman et al., 2004; Sarkar

et al., 2015; Tovey et al., 2021) in the Lac de Gras kimberlite field include the Darkwing (75.2 ± 21.6 Ma), Kudu (73.7 ± 7.4 Ma), C13 (73.9 ± 2.6 Ma), Jaeger (71.4 ± 7.8 Ma), and Hardy Lake kimberlites (73–71 Ma), all of which are slightly younger (Campanian–Maastrichtian) than the Wombat maar lacustrine sediment age inferred from the tephra zircon U-Pb age.

5.2.2. The Wombat Maar Tephra Geochemistry and Potential Source Regions

The volcanic source(s) of the tephra recovered from the Wombat maar cores are unknown. Wombat tephra samples UA3135 and UA3134 are very fine rhyolites with trace element compositions pointing to an origin in an active continental margin or oceanic arc (Fig. 11). The Okhotsk-Chukotka Volcanic Belt is a subduction-related magmatic province in NE Eurasia that is located on the western coast of the Sea of Okhotsk to the east of the Chukchi Peninsula. The belt is characterized by voluminous high-silica magmatism ($SiO_2 \geq 80$ vol%), with the most recent eruptions occurring at ca. 82–79 Ma (Campanian; Tikhomirov et al., 2012; Pease et al., 2018). The zircon U-Pb ages of the rhyolitic ignimbrites of the western Okhotsk flank zone of the Okhotsk-Chukotka Volcanic Belt suggest the occurrence of volcanism from the Coniacian (89.8 Ma) to the Campanian–Maastrichtian boundary (72.1 Ma; Tikhomirov et al., 2012), which is contemporaneous with the Wombat tephra zircon U-Pb ages. The Okhotsk-Chukotka Volcanic Belt is presently located >2500 km NW of the Wombat locality and requires very intense, large-scale Plinian-type volcanism for tephra to reach the Lac de Gras region. Prevailing winds would plausibly transport a tephra plume from the Okhotsk-Chukotka Volcanic Belt eastward toward the Lac de Gras region in northern North America, which is consistent with the lack of Okhotsk-Chukotka Volcanic Belt tephra deposits west of the source region (Spicer and Herman, 2010). Based on their geochemistry, the distal nature of the glass, and paleo-wind inferences, it is possible that the eruption source area for the Wombat tephra beds is the Okhotsk-Chukotka Volcanic Belt, although other sources (e.g., Coast arc, Kluane arc, Idaho batholiths, and Hansen Point Volcanic Complex) cannot be discounted. The sparse availability of reliable geochemical and geochronological data for Upper Cretaceous tephra deposits in northern North America is a major hurdle for reliable correlation of these distal tephra beds, despite their potential applicability as tephrostratigraphic marker horizons, for example, in the Cretaceous strata of the Western Canadian Sedimentary Basin (e.g., Lerbekmo, 1968).

5.2.3. Implications for Arctic Pollen-Based Biostratigraphy

Given the Late Cretaceous (early Campanian) age of lacustrine sedimentation in the Wombat pipe maar sediments reported here, it is notable that *Aquilapollenites* and *Wodehouseia* are absent from Wombat palynological samples. These taxa are typical elements in Upper Cretaceous strata situated within the *Aquilapollenites* floral province that occupied the northern and western parts of North America, from at least northern New Mexico northward to the Arctic islands and Alaska (Batten, 1984). Similarly, some taxa in the Wombat lacustrine sediments (e.g., *Alnipollenites* and *Ericaceiopollenites*) are commonly associated with Cenozoic strata, which is seemingly inconsistent with the 80.9 ± 1.0 Ma early Campanian, tephra-based age constraint for the Wombat maar.

The occurrence of *Aquilapollenites* pollen is diachronous in North America. In the Western Canadian Sedimentary Basin, this taxon appears in the Santonian (Braman and Sweet, 2012), and is later represented by a diversity of forms in the Campanian and Maastrichtian, even at high northern latitudes (Stanley, 1970; Batten, 1984). Diachroneity of its occurrence is noted within strata of western Canada (e.g., Braman, 2001). *Aquilapollenites*, for example, is rare in the Upper Santonian to lower Campanian Milk River Formation in southern Alberta (Braman, 2001), and absent from correlative strata in the Rocky Mountain region in the United States (Nichols, 1994). In southern Alberta, species of *Aquilapollenites* pollen do not become common until within the fully marine Campanian Pakowki Formation and younger units, where *Aquilapollenites* becomes characteristic of the Pakowki and Foremost formations across much of the Western Interior Basin (Braman, 2001, 2018). At other localities in the Western Canadian Sedimentary Basin, *Aquilapollenites* taxa are present in Coniacian (*A. rombicus*, *A.* species 1 of Braman and Sweet, 2012) and Santonian-aged strata (*A. senonicus*; Braman and Sweet, 2012). *Aquilapollenites* spp. are part of the Early Loranthaceous Palynofloral suite of Norris et al. (1975), and present in strata of likely Santonian to Late Campanian age (Lea Park Formation; Amoco B-1 Youngstown well, Alberta).

The diachroneity of *Aquilapollenites* occurrences inhibits correlation within the *Aquilapollenites* Floral Province of Canada, eastern Russian, and northern China for the Late Cretaceous (Braman, 2001). In contrast, *Wodehousiea* pollen, another Upper Cretaceous indicator, is typically confined to the Maastrichtian in North America and eastern Asia (Nichols and Jacobson, 1982, and references therein; Nichols et al., 2010), but rare occurrences in the Campanian are noted. For example, *Wodehouseia* pollen (*W. avita* and *W. spinata*) occurs in uppermost Maastrichtian strata in the Canadian Western Interior Sedimentary Basin, and as *W. fimbriata, W. spinulosus, W. gracile,* and *W. jacutense* in strata of Maastrichtian age in the Horton River area of the Northwest Territories (above 170 ft in section CR16B; McIntyre, 1974). Both *Wodehouseia* and *Aquilapollenties* pollen occur in strata of Maastrichtian age in the Yukon Territory (Sweet, 1978), and are dominant elements in Maastrichtian strata on the Ellef Ringnes and Amund Ringnes islands in the Canadian Arctic Archipelago (Hopkins, 1973). However, *W. edmontonicola* is also documented in strata dated to ca. 73 Ma (Campanian; Braman and Sweet, 2012), and *W. gracile* is documented in rocks of uppermost Campanian age (ca. 73 Ma) in southern Alberta (Braman, 2018). The occurrence of *Alnipollenites* and *Ericaceiopollenites* pollen is typically indicative of a Paleocene age; however, both are known to occur in the Cretaceous (e.g., Takahashi, 1974; Miki, 1977; Hickey et al., 1983; Crane and Stockey, 1987). Therefore, the absence of *Aquilapollenites* and *Wodehousiea* pollen in samples processed from the DDH00-5 and CH93-95 cores from the Wombat kimberlite maar sediments accommodates a Campanian age determination based on the U-Pb age determination of the tephra at 233.9 VE m depth in core DDH00-5.

5.2.4. Implications for Late Cretaceous Paleogeography of the Western Interior Seaway

During most of the Cretaceous, the Western Interior Seaway covered a vast portion of North America (Fig. 12), spanning more than 6000 km from the Gulf of Mexico to the Arctic Ocean with a width of >1600 km at its maximum extent (Leckie et al., 1991; Hay, 1995). Broad swaths of the western Canadian Shield, such as the Lac de Gras region, are devoid of known Phanerozoic sedimentary rocks (Ault et al., 2013), which makes it difficult to infer the extent of the Western Interior Seaway in those areas. Though Phanerozoic rocks were recovered as xenoliths reworked into kimberlite (e.g., Sweet et al., 2003; Stasiuk et al., 2003, 2006), the Wombat maar sediments represent the only intact Upper Cretaceous sedimentary record in the Lac de Gras region, which makes it a most valuable record for this time period.

Vitrinite reflectance and apatite (U-Th)/He thermochronometry suggest that the Lac de Gras region was covered by Cretaceous strata ranging between 1.4 km and 2.7 km thick (Stasiuk et al., 2002; Ault et al., 2013). Palynological investigation of sedimentary xenoliths recovered from kimberlite crater-facies in other

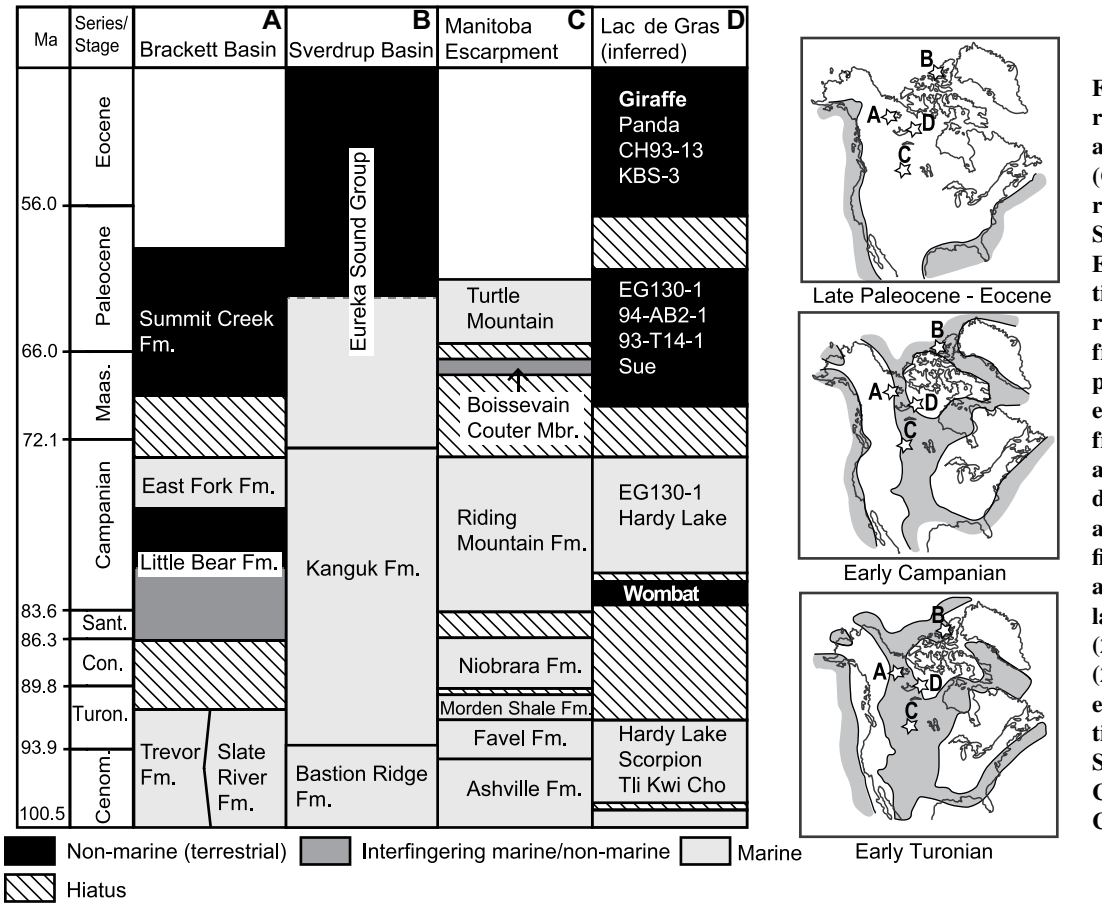

Figure 12. Western Interior Seaway paleogeography and schematic Cenomanian (Cenom.) to Eocene stratigraphy for the Brackett Basin, Sverdrup Basin, and Manitoba Escarpment, and inferred stratigraphy for the Lac de Gras region. Stratigraphy is adapted from Sweet et al. (2003), and paleogeography of the Western Interior Seaway is adapted from Schröder-Adams (2014, and references therein). Additional sedimentary xenoliths and maar lake sedimentary fill data are from Nassichuk and McIntyre (1996); McKinlay et al. (1998); Stasiuk et al. (2002); and Stasiuk et al. (2006). Time scale is after Gale et al. (2020). Stars indicate locations of stratigraphic columns. Sant.—Santonian; Con.—Coniacian; Turon.—Turonian; Cenom.—Cenomanian.

Lac de Gras kimberlites provides further context regarding the inferred stratigraphic order in the region. Between ca. 105 Ma and 90 Ma, palynomorph assemblages and kerogen types in kimberlite sedimentary xenoliths indicate a marine or marginal marine depositional environment, which suggests that the Lac de Gras area was near sea level at this time (Nassichuk and McIntyre, 1996; McKinlay et al., 1998; Stasiuk et al., 2002; Sweet et al., 2003). Sedimentary xenoliths dating between ca. 90 Ma and 80 Ma are only encountered in Hardy Lake kimberlites, which contain terrestrial Type III kerogen, but likely with significant reworking and recycling of organic matter (Stasiuk et al., 2002). During this time, Sweet et al. (2003) suggested a significant hiatus in deposition due to the absence of age-indicative pollen assemblages.

The Wombat lacustrine fill indicates that during the early Campanian, the Western Interior Seaway regressed, and the Lac de Gras area was above sea level. Organic petrological, geochemical, and palynological data from sample EG130-1 and Hardy Lake kimberlite xenoliths suggest that the Western Interior Seaway likely transgressed again during the Late Campanian, submerging the Lac de Gras region and causing marine conditions, followed by a hiatus between ca. 73 Ma and 69 Ma (McKinlay et al., 1998; Stasiuk et al., 2002; Sweet et al., 2003). Xenoliths from kimberlites EG130-1, AB2, and T14, and post-eruptive sedimentary fills from the Panda, Sue, and KB-3 pipes suggest that nonmarine conditions then occurred between ca. 69 Ma and 45 Ma, with a gap in the record between ca. 61 Ma and 56 Ma (McKinlay et al., 1998; Stasiuk et al., 2002; Hamblin et al., 2003; Sweet et al., 2003; Wolfe et al., 2012). This is consistent with the revised chronological framework for the Giraffe maar sediments, which indicates nonmarine conditions in Lac de Gras at ca. 48 Ma. At some point after ca. 45 Ma, most of the Cretaceous strata must have been eroded away by river systems (Bell, 1895; Duk-Rodkin and Hughes, 1994) or were preserved only locally as xenoliths in kimberlite or kimberlitic maar lake fills.

Regional correlation of marine and nonmarine sedimentation between contemporaneous units along the Manitoba Escarpment, Brackett Basin, and Sverdrup Basin, together with inferred stratigraphy in the Lac de Gras area, provide a broader perspective on the paleogeography of the Western Interior Seaway (Fig. 12). The Brackett Basin, ~650 km WNW of the Wombat locality, is the closest terrestrial sedimentary succession to the Lac de Gras area (Sweet et al., 1989). The Little Bear Formation in the Brackett Basin was interpreted as a series of delta-front or propagating shoreface deposits, and it contains both marine and nonmarine strata and is roughly contemporaneous to the Wombat maar sedimentary fill (Dixon, 1999). The underlying and overlying Slate River/Trevor (Cenomanian–Turonian) and East Fork (Campanian–Maastrichtian) formations are characterized as marine deposits, which suggests a Turonian regression of the Western Interior Seaway and transgression sometime in the Late Campanian (Yorath and Cook, 1981).

The Manitoba Escarpment is a mostly marine Cretaceous sedimentary succession located ~1300 km SE of the Lac de Gras region (Fig. 12), roughly along depositional strike. The Cenomanian to upper Campanian formations in the Manitoba Escarpment were deposited in a marine setting near the eastern margin of the Western Canada Sedimentary Basin (Schröder-Adams et al., 2001). The Upper Maastrichtian to Paleocene Boissevain Court and Turtle Mountain formations are mainly nonmarine and rep-

resent final regression of the Western Interior Seaway in the region.

The Sverdrup Basin is a rift basin located among the Queen Elizabeth Islands and inter-island channels ∼1500 km NE of the Lac de Gras region (Fig. 12; Miall, 1991; Ricketts, 1994). The Cretaceous strata of the Bastion Ridge Formation (where it occurs), the Kanguk Formation, and the Mount Lawson and lower section of the terrestrial Eureka Sound Group combined Margaret formations (= Strand Bay Formation) are predominantly marine in origin and together span the Cenomanian to early/middle Paleocene, which suggests the region was below sea level for most of the Late Cretaceous (Miall, 1991; Ricketts, 1994; Embry and Beauchamp, 2019). By the middle/late Paleocene, the area had uplifted and was predominately nonmarine, as indicated by numerous well-preserved plant fossils in the Mount Moore Formation and Margaret Formation (= Iceberg Bay Formation) within the Eureka Sound Group on Ellesmere Island (West et al., 2019).

The ages and depositional environments of stratigraphic successions in the Brackett Basin, Manitoba Escarpment, and Sverdrup Basin, together with the xenolith and kimberlite sedimentary records from the Lac de Gras area, make it possible to infer patterns of regression-transgression of the northern reaches of the Western Interior Seaway shoreline (Fig. 12). Marine conditions persisted at all of the localities from Cenomanian to at least middle Turonian time, followed by hiatuses in the Brackett Basin and Lac de Gras that lasted at least until the Late Santonian. A lower Campanian section of the Little Bear Formation and the Wombat maar lake sediments both contain terrestrial sedimentary and palynological terrestrial indicators that suggest at least a regional narrowing of the Western Interior Seaway and a shift to a nonmarine environment at the Lac de Gras site, while the Manitoba Escarpment likely experienced a hiatus in deposition, and Sverdrup Basin remained below sea level. The subsequent middle Late Campanian transgression of the Western Interior Seaway reversed conditions back to the full/marginal marine environment in the Lac de Gras region and the Brackett Basin. The timing of the final shift from marine to permanent terrestrial setting in the Lac de Gras region is unclear but probably occurred sometime in the Late Maastrichtian to early Paleocene.

6. CONCLUSION

The combination of CA-ID-TIMS and LA-ICP-MS U-Pb zircon dating of tephra was used to determine the timing of the Giraffe maar lacustrine sediments, yielding age estimates of $47.995 \pm 0.082|0.087$ Ma and $48.72 \pm 0.29|0.30$ Ma for the upper and lower lacustrine successions, respectively. Taken together with the Rb-Sr phlogopite emplacement age of 47.8 ± 1.4 Ma, the radiometric geochronology suggests that the Giraffe maar infill was deposited at the end of the early Eocene (Ypresian). The existing paleoclimatic and atmospheric CO_2 proxy reconstructions from the Giraffe maar sediments are thus ∼10 m.y. older than previously thought.

The geochronology of the Wombat maar sediments, as determined by zircon LA-ICP-MS U-Pb dating of a distal rhyolitic tephra bed found near the base of the lacustrine succession, yields a close minimum age for the onset of deposition at 80.9 ± 1.0 Ma (early Campanian). No estimate of the eruption age of the Wombat kimberlite is currently available. Pollen biostratigraphy of the Wombat maar fill is complicated by the heterochronicity of standard Late Cretaceous and Paleocene indicator taxa; nevertheless, the biostratigraphic constraints do not contradict the ca. 81 Ma early Campanian age based on tephra zircon U-Pb dating. The Wombat maar sediments are the only record of the early Campanian terrestrial strata in Lac de Gras. They provide a paleoenvironmental snapshot that supplements the limited information from xenoliths of now-eroded Mesozoic cover rock in the Lac de Gras kimberlites. Together with sediments from basins elsewhere in mid-continental Canada, the Wombat maar sediment provides new insight into the Late Cretaceous and Paleogene paleogeography of a data-poor region of the Western Interior Seaway.

The eruptive source of the Giraffe and Wombat tephra beds is unclear, with the glass geochemistry being compatible with an origin in an active continental margin or oceanic arc, but sample UA2845 suggests that an intracontinental system cannot be ruled out. Potential tephra sources include the Late Cretaceous Okhotsk-Chukotka Volcanic Belt for the Wombat maar sediments and the Paleocene rhyolitic-welded ignimbrites in east-central Alaska for the Giraffe maar locality.

Both the early Eocene Giraffe and Upper Cretaceous Wombat post-eruptive maar lake sediments preserve a diversity of fossil and sedimentary data that provide a window into subarctic environments during past globally warm climatic intervals (Siver and Lott, 2023). With hundreds of known kimberlite pipes in the Lac de Gras field, most of which are latest Cretaceous or Paleogene in age, it is likely that there are other kimberlite maar sedimentary records of subarctic greenhouse paleoenvironments. The refined chronological framework provided in this study is a required first step for the development of proxy paleoclimatic records from the long, continuous sedimentary records of these high-latitude kimberlite maars. In turn, the new geochronology will enhance the utility of these paleoclimatic data for proxy-model comparison, for constraining, pole-to-equator climatic gradients, and for elucidating the function of the greenhouse climatic system in deep time at higher latitudes.

7. ACKNOWLEDGMENTS

We thank Barrett Elliott (Northwest Territories Geological Survey) for facilitating access to core DDH00-5, Richard Fontaine (Geological Survey of Canada) for access to core BHP99-01, and Anne-Marie Lizarralde for assistance with sampling core CH93-29. The research was funded by Natural Sciences and Engineering Research Council of Canada Discovery Grants and Northern Research Supplements to A. Reyes, B.J.L. Jensen, J.H.F.L. Davies, and J.A. Westgate; National Science Foundation grants EAR-1725265 and EAR-1940070 to P.A. Siver; and a Canada Excellence Research Chair held by D.G. Pearson, which supports analyses at the University of Alberta Arctic Resources Geochemistry Laboratory. C.K. West thanks a private donor for funding the Climates of the Canadian North Postdoctoral Fellowship at the University of Alberta. Palynological analysis and interpretation by J.M. Galloway supports the Geological Survey of Canada's GEM GeoNorth Program, and this contribution represents NRCan contribution number 20230003. Eva Koppelhus provided important early insight into the palynology of the Wombat kimberlite pipe. We thank David Barbeau and Jennifer Kasbohm for their insightful and constructive reviews of the manuscript.

REFERENCES CITED

Anagnostou, E., et al., 2020, Proxy evidence for state-dependence of climate sensitivity in the Eocene greenhouse: Nature Communications, v. 11, 4436, https://doi.org/10.1038/s41467-020-17887-x.

Ault, A.K., Flowers, R.M., and Bowring, S.A., 2013, Phanerozoic surface history of the Slave Craton: Tectonics, v. 32, p. 1066–1083, https://doi.org/10.1002/tect.20069.

Bacon, C.R., Foster, H.L., and Smith, J.G., 1990, Rhyolitic calderas of the Yukon-Tanana Terrane, east central Alaska: Volcanic remnants of a Mid-Cretaceous magmatic arc: Journal of Geophysical Research: Solid Earth, v. 95, p. 21,451–21,461, https://doi.org/10.1029/JB095iB13p21451.

Barber, A., Siver, P.A., and Karis, W., 2013, Euglyphid testate amoebae (Rhizaria: *Euglyphida*) from an Arctic Eocene waterbody: Evidence of evolutionary stasis in plate morphology for over 40 million years: Protist, v. 164, p. 541–555, https://doi.org/10.1016/j.protis.2013.05.001.

Batten, D.J., 1984, Palynology, climate and the development of Late Cretaceous floral provinces in the Northern Hemisphere; a review, *in* Brenchley, P., ed., Fossils and Climate: Wiley, p. 127–164.

Bell, R., 1895, A great pre-glacial river in northern Canada: Scottish Geographical Magazine, v. 11, p. 368.

Bowring, S.A., and Williams, I.S., 1999, Priscoan (4.00–4.03 Ga) orthogneisses from northwestern Canada: Contributions to Mineralogy and Petrology, v. 134, p. 3–16, https://doi.org/10.1007/s004100050465.

Boxer, G.L., Lorenz, V., and Smith, C.B., 1986, Geology and volcanology of the Argyle (AK1) lamproite diatreme: International Kimberlite Conference: Extended Abstracts, v. 4, p. 21–23, https://doi.org/10.29173/ikc1060.

Braman, D.R., 2001, Terrestrial palynomorphs of the Upper Santonian–?lowest Campanian Milk River Formation,

Southern Alberta, Canada: Palynology, v. 25, p. 57–107, https://doi.org/10.1080/01916122.2001.9989556.

Braman, D.R., 2018, Terrestrial palynostratigraphy of the Upper Cretaceous (Santonian) to lowermost Paleocene of southern Alberta, Canada: Palynology, v. 42, p. 102–147, https://doi.org/10.1080/01916122.2017.1311958.

Braman, D.R., and Sweet, A.R., 2012, Biostratigraphically useful Late Cretaceous–Paleocene Terrestrial palynomorphs from the Canadian Western Interior Sedimentary Basin: Palynology, v. 36, p. 8–35, https://doi.org/10.1080/01916122.2011.642127.

Brideaux, W.W., and McIntyre, D.J., 1975, Miospores and Microplankton from Aptian-Albian Rocks along Horton River, District of Mackenzie: Geological Survey of Canada Bulletin 252, 97 p., https://doi.org/10.4095/103972.

Brothers, S., Vermaire, J.C., and Gregory-Eaves, I., 2008, Empirical models for describing recent sedimentation rates in lakes distributed across broad spatial scales: Journal of Paleolimnology, v. 40, p. 1003–1019, https://doi.org/10.1007/s10933-008-9212-8.

Buryak, S.D., 2020, Geochronology and bulk sediment geochemistry of the Late Cretaceous maar lake sedimentary fill of the Wombat kimberlite pipe, subarctic Canada [M.Sc. thesis]: Edmonton, University of Alberta, 101 p., https://doi.org/10.7939/r3-9dsr-wh73.

Coble, M.A., and Mahood, G.A., 2016, Geology of the High Rock caldera complex, northwest Nevada, and implications for intense rhyolitic volcanism associated with flood basalt magmatism and the initiation of the Snake River Plain–Yellowstone trend: Geosphere, v. 12, p. 58–113, https://doi.org/10.1130/GES01162.1.

Condon, D.J., Schoene, B., McLean, N.M., Bowring, S.A., and Parrish, R.R., 2015, Metrology and traceability of U-Pb isotope dilution geochronology (EARTHTIME Tracer Calibration Part I): Geochimica et Cosmochimica Acta, v. 164, p. 464–480, https://doi.org/10.1016/j.gca.2015.05.026.

Cookenboo, H.O., Orchard, M.J., and Daoud, D.K., 1998, Remnants of Paleozoic cover on the Archean Canadian Shield: Limestone xenoliths from kimberlite in the central Slave Craton: Geology, v. 26, p. 391–394, https://doi.org/10.1130/0091-7613(1998)026<0391:ROPCOT>2.3.CO;2.

Crane, P.R., and Stockey, R.A., 1987, Betula leaves and reproductive structures from the Middle Eocene of British Columbia, Canada: Canadian Journal of Botany, v. 65, p. 2490–2500, https://doi.org/10.1139/b87-338.

Crann, C.A., Patterson, R.T., Macumber, A.L., Galloway, J.M., Roe, H.M., Blaauw, M., Swindles, G.T., and Flack, H., 2015, Sediment accumulation rates in subarctic lakes: Insights into age-depth modeling from 22 dated lake records from the Northwest Territories, Canada: Quaternary Geochronology, v. 27, p. 131–144, https://doi.org/10.1016/j.quageo.2015.02.001.

Creaser, R.A., Gütter, H., Carlson, J., and Crawford, B., 2004, Macrocrystal phlogopite Rb-Sr dates for the Ekati property kimberlites, Slave Province, Canada: Evidence for multiple intrusive episodes in the Paleocene and Eocene: Lithos, v. 76, p. 399–414, https://doi.org/10.1016/j.lithos.2004.03.039.

Dixon, J., 1999, Mesozoic–Cenozoic Stratigraphy of the Northern Interior Plains and Plateaux, Northwest Territories: Geological Survey of Canada Bulletin 536, 56 p., https://doi.org/10.4095/210800.

Donovan, J.J., Kremser, D., Fournelle, J.H., and Goemann, K., 2015, Probe for EPMA: Acquisition, automation and analysis, version 11: Eugene, Oregon, Probe Software Inc., http://www.probesoftware.com (accessed June 2019).

Doria, G., Royer, D.L., Wolfe, A.P., Fox, A., Westgate, J.A., and Beerling, D.J., 2011, Declining atmospheric CO_2 during the late middle Eocene climate transition: American Journal of Science, v. 311, p. 63–75, https://doi.org/10.2475/01.2011.03.

Duk-Rodkin, A., and Hughes, O.L., 1994, Tertiary–Quaternary drainage of the pre-glacial Mackenzie basin: Quaternary International, v. 22–23, p. 221–241, https://doi.org/10.1016/1040-6182(94)90015-9.

Edwards, C.B., and Howkins, J.B., 1966, Kimberlites in Tanganyika with special reference to the Mwadui occurrence: Economic Geology, v. 61, p. 537–554, https://doi.org/10.2113/gsecongeo.61.3.537.

Eldrett, J.S., Greenwood, D.R., Harding, I.C., and Huber, M., 2009, Increased seasonality through the Eocene to Oligocene transition in northern high latitudes: Nature, v. 459, p. 969–973, https://doi.org/10.1038/nature08069.

Embry, A., and Beauchamp, B., 2019, Sverdrup Basin, *in* Miall, A.D., ed., The Sedimentary Basins of United States and Canada: Elsevier, p. 559–592, https://doi.org/10.1016/B978-0-444-63895-3.00014-0.

Field, M., Gibson, J.G., Wilkes, T.A., Gababotse, J., and Khujwe, P., 1995, The geology of the Orapa A/K1 kimberlite, Botswana: Further insight into the emplacement of kimberlite pipes: International Kimberlite Conference: Extended Abstracts, v. 6, p. 155–157.

Fisher, R.V., and Schmincke, H.-U., 1984, Alteration of volcanic glass, *in* Fisher, R.V., and Schmincke, H.-U., eds., Pyroclastic Rocks: Springer-Verlag, p. 312–345, https://doi.org/10.1007/978-3-642-74864-6_12.

Gale, A.S., Mutterlose, J., Batenburg, S., Gradstein, F.M., Agterberg, F.P., Ogg, J.G., and Petrizzo, M.R., 2020, Chapter 27—The Cretaceous Period, *in* Gradstein, F.M., Ogg, J.G., Schmitz, M.D., and Ogg, G.M., eds., Geologic Time Scale 2020: Elsevier, p. 1023–1086, https://doi.org/10.1016/B978-0-12-824360-2.00027-9.

Galloway, J.M., Bringué, M., Buryak, S.D., Reyes, A.V., West, C.K., and Siver, P.A., 2022, Palynological Analyses of Maar Lake Sediments from Core Samples of Wombat Kimberlite Pipe, Northwest Territories, Canada: Geological Survey of Canada Open File 8864, 29 p., https://doi.org/10.4095/329615.

Gansecki, C.A., Mahood, G.A., and McWilliams, M., 1998, New ages for the climactic eruptions at Yellowstone: Single-crystal $^{40}Ar/^{39}Ar$ dating identifies contamination: Geology, v. 26, p. 343–346, https://doi.org/10.1130/0091-7613(1998)026<0343:NAFTCE>2.3.CO;2.

Giuliani, A., and Pearson, D.G., 2019, Kimberlites: From deep Earth to diamond mines: Elements, v. 15, p. 377–380, https://doi.org/10.2138/gselements.15.6.377.

Grande, T.C., Wilson, M.V.H., Reyes, A.V., Buryak, S.D., Wolfe, A.P., and Siver, P.A., 2022, A new, Late Cretaceous gonorynchiform fish in the genus †*Notogoneus* from drill core of crater-lake deposits in a kimberlite maar, Northwest Territories, Canada: Cretaceous Research, v. 135, https://doi.org/10.1016/j.cretres.2022.105176.

Greenwood, D.R., Basinger, J.F., and Smith, R.Y., 2010, How wet was the Arctic Eocene rain forest?: Estimates of precipitation from Paleogene Arctic macrofloras: Geology, v. 38, p. 15–18, https://doi.org/10.1130/G30218.1.

Grimm, E., 1993, TILIA: A pollen program for analysis and display: Springfield, Illinois State Museum.

Hamblin, A.P., 2015, An Eocene Post-Kimberlite Maar Lake: Lacustrine Oil-Shale Crater-Fill Deposits, Lac de Gras Area, Northwest Territories, Canada: Geological Survey of Canada Open File 7809, 26 p., https://doi.org/10.4095/296430.

Hamblin, A.P., Stasiuk, L.D., Sweet, A.R., Lockhart, G.D., Dyck, D.R., Jagger, K., and Snowdon, L.R., 2003, Post-kimberlite Eocene strata within a crater basin, Lac de Gras, Northwest Territories, Canada: International Kimberlite Conference, Extended Abstracts, v. 8, p. 1–5, https://doi.org/10.29173/ikc3015.

Hawthorne, J.B., 1975, Model of a kimberlite pipe: Physics and Chemistry of the Earth, v. 9, p. 1–15, https://doi.org/10.1016/0079-1946(75)90002-6.

Hay, W.W., 1995, Paleoceanography of marine organic-carbon-rich sediments, *in* Huc, A.Y., ed., Paleogeography, Paleoclimate, and Source Rocks: American Association of Petroleum Geologists Studies in Geology 40, p. 21–59, https://doi.org/10.1306/St40595C2.

Heaman, L.M., Kjarsgaard, B.A., and Creaser, R.A., 2004, The temporal evolution of North American kimberlites: Lithos, v. 76, p. 377–397, https://doi.org/10.1016/j.lithos.2004.03.047.

Hickey, L.J., West, R.M., Dawson, M.R., and Choi, D.K., 1983, Arctic terrestrial biota: Paleomagnetic evidence of age disparity with mid-northern latitudes during the Late Cretaceous and early Tertiary: Science, v. 221, p. 1153–1156, https://doi.org/10.1126/science.221.4616.1153.

Hiess, J., Condon, D.J., McLean, N., and Noble, S.R., 2012, $^{238}U/^{235}U$ systematics in terrestrial-bearing minerals: Science, v. 335, p. 1610–1614, https://doi.org/10.1126/science.1215507.

Hopkins, W.S., 1973, Some preliminary palynological conclusions on the Albian and Upper Cretaceous strata of Amund and Ellef Ringnes Islands, District of Franklin, *in* Blackadar, R.G., ed., Report of Activities, Part B: November 1971 to March 1972: Geological Survey of Canada Paper 73-1B, 129 p., https://doi.org/10.4095/119831.

Hu, S., Hickey, L., Siver, P.A., and Wolfe, A.P., 2011, Palynology and age of post-eruptive lake sediments from the Wombat kimberlite locality, Northwest Territories, Canada: Geological Society of America Abstracts with Programs, v. 43, no. 5, p. 157.

Jackson, S.E., Pearson, N.J., Griffin, W.L., and Belousova, E.A., 2004, The application of laser ablation–inductively coupled plasma–mass spectrometry to in situ U-Pb zircon geochronology: Chemical Geology, v. 211, p. 47–69, https://doi.org/10.1016/j.chemgeo.2004.06.017.

Jaques, A.L., Lewis, J.D., and Smith, C.B., 1986, The Kimberlites and Lamproites of Western Australia: Geological Survey of Western Australia Bulletin 132, 268 p.

Jensen, B.J.L., et al., 2021, A latest Pleistocene and Holocene composite tephrostratigraphic framework for northeastern North America: Quaternary Science Reviews, v. 272, https://doi.org/10.1016/j.quascirev.2021.107242.

Inglis, G.N., et al., 2020, Global mean surface temperature and climate sensitivity of the early Eocene Climatic Optimum (EECO), Paleocene–Eocene Thermal Maximum (PETM), and latest Paleocene: Climate of the Past, v. 16, p. 1953–1968, https://doi.org/10.5194/cp-16-1953-2020.

Keller, C.B., Schoene, B., and Samperton, K.M., 2018, A stochastic sampling approach to zircon eruption age interpretation: Geochemical Perspectives Letters, v. 8, https://doi.org/10.7185/geochemlet.1826.

Klepeis, K.A., Crawford, M.L., and Gehrels, G., 1998, Structural history of the crustal-scale Coast shear zone north of Portland Canal, southeast Alaska and British Columbia: Journal of Structural Geology, v. 20, p. 883–904, https://doi.org/10.1016/S0191-8141(98)00020-0.

Kohn, B.P., Pillans, B., and McGlone, M.S., 1992, Zircon fission track age for middle Pleistocene Rangitawa Tephra, New Zealand: Stratigraphic and paleoclimatic significance: Palaeogeography, Palaeoclimatology, Palaeoecology, v. 95, p. 73–94, https://doi.org/10.1016/0031-0182(92)90166-3.

Krogh, T.E., 1973, A low-contamination method for hydrothermal decomposition of zircon and extraction of U and Pb for isotopic age determinations: Geochimica et Cosmochimica, v. 37, p. 485–494, https://doi.org/10.1016/0016-7037(73)90213-5.

Kuehn, S.C., Froese, D.G., and Shane, P.A.R., 2011, The INTAV intercomparison of electron-beam microanalysis of glass by tephrochronology laboratories: Results and recommendations: Quaternary International, v. 246, p. 19–47, https://doi.org/10.1016/j.quaint.2011.08.022.

Le Bas, M.J., LeMaitre, R.W., Streckeisen, A., and Zanettin, B., 1986, A chemical classification of volcanic rocks based on the total alkali-silica diagram: Journal of Petrology, v. 27, p. 745–750, https://doi.org/10.1093/petrology/27.3.745.

Leckie, D.A., Potocki, D.J., and Visser, K., 1991, The Lower Cretaceous Chinkeh Formation: A frontier-type play in the Liard Basin of western Canada (1): AAPG Bulletin, v. 75, p. 1324–1352, https://doi.org/10.1306/0C9B2943-1710-11D7-8645000102C1865D.

Lenz, O.K., Wilde, V., Mertz, D.F., and Riegel, W., 2015, New palynology-based astronomical and revised $^{40}Ar/^{39}Ar$ ages for the Eocene maar lake of Messel (Germany): International Journal of Earth Sciences, v. 104, p. 873–889, https://doi.org/10.1007/s00531-014-1126-2.

Lerbekmo, J.F., 1968, Chemical and modal analyses of some Upper Cretaceous and Paleocene bentonites from western Alberta: Canadian Journal of Earth Sciences, v. 5, p. 1505–1511, https://doi.org/10.1139/e68-147.

Liang, J.-Q., Leng, Q., Höfig, D.F., Niu, G., Wang, L., Royer, D.L., Burke, K., Xiao, L., Zhang, Y.G., and Yang, H., 2022, Constraining conifer physiological parameters in leaf gas-exchange models for ancient CO_2 reconstruction:

Global and Planetary Change, v. 209, https://doi.org/10.1016/j.gloplacha.2022.103737.

Mahon, K.I., 1996, The New "York" regression: Application of an improved statistical method to geochemistry: International Geology Review, v. 38, p. 293–303, https://doi.org/10.1080/00206819709465336.

McIntyre, D.J., 1974, Palynology of an Upper Cretaceous Section, Horton River, District of Mackenzie, N.W.T.: Geological Survey of Canada Paper 74-14, 57 p., https://doi.org/10.4095/103304.

McKinlay, F.T., Scott Smith, B.H., de Gasparis, S., and Kong, J., 1998, Geology of the recently discovered Hardy Lake kimberlites, NWT: International Kimberlite Conference, Extended Abstracts, v. 7, p. 564–566, https://doi.org/10.29173/ikc2805.

McLean, N.M., Bowring, J.F., and Bowring, S.A., 2011, An algorithm for U-Pb isotope dilution data reduction and uncertainty propagation: U-Pb ALGORITHM: Geochemistry, Geophysics, Geosystems, v. 12, https://doi.org/10.1029/2010GC003478.

Miall, A.D., 1991, Late Cretaceous and Tertiary basin development and sedimentation, Arctic Islands, *in* Trettin H.P., ed., Geology of the Innuitian Orogen and Arctic Platform of Canada and Greenland: Geological Society of America, Decade of North American Geology, Geology of North America, v. 3, p. 437–458, https://doi.org/10.1130/DNAG-GNA-E.435.

Miki, A., 1977, Late Cretaceous pollen and spore floras of northern Japan: Composition and interpretation: Journal of the Faculty of Science, Hokkaido University, Series 4, Geology and Mineralogy, v. 17, p. 399–436.

Mingram, J., 1998, Laminated Eocene maar-lake sediments from Eckfeld (Eifel region, Germany) and their short-term periodicities: Palaeogeography, Palaeoclimatology, Palaeoecology, v. 140, p. 289–305, https://doi.org/10.1016/S0031-0182(98)00021-2.

Moss, S., Russell, J.K., and Andrews, G.D.M., 2008, Progressive infilling of a kimberlite pipe at Diavik, Northwest Territories, Canada: Insights from volcanic facies architecture, textures, and granulometry: Journal of Volcanology and Geothermal Research, v. 174, p. 103–116, https://doi.org/10.1016/j.jvolgeores.2007.12.020.

Nassichuk, W.W., and Dyck, D.R., 1998, Fossils recovered from kimberlite pipes in the Lac de Gras field, Slave province, northwest Canada: Geological implications: International Kimberlite Conference, Extended Abstracts, v. 7, p. 612–614, https://doi.org/10.29173/ikc2822.

Nassichuk, W.W., and McIntyre, D.J., 1996, Fossils from diamondiferous kimberlites at Lac de Gras, NWT: Age and paleogeography, *in* LeCheminant, A.N., Richardson, D.G., Dolabio R.N.W., and Richardson K.A., eds., Searching for Diamonds in Canada: Geological Survey of Canada Open File 3228, p. 43–46.

Nichols, D.J., 1994, A revised palynostratigraphic zonation of the nonmarine Upper Cretaceous, Rocky Mountain Region, United States, *in* Caputo, M.V., Peterson, J.A., and Franczyk, K.J., eds., Mesozoic Systems of the Rocky Mountain Region, USA: SEPM (Society for Sedimentary Geology), Rocky Mountain Section, p. 503–520.

Nichols, D.J., and Jacobson, S.R., 1982, Palynostratigraphic framework for the Cretaceous (Albian–Maastrichtian) of the overthrust belt of Utah and Wyoming: Palynology, v. 6, p. 119–147, https://doi.org/10.1080/01916122.1982.9989238.

Nichols, D.J., Matsukawa, M., and Ito, M., 2010, The geological age and phytogeographical significance of some metamorphosed palynomorphs from the Omichidani Formation of Japan: Palynology, v. 34, p. 157–163, https://doi.org/10.1080/01916121003672941.

Nixon, P.H., 1995, The morphology and nature of primary diamondiferous occurrences: Journal of Geochemical Exploration, v. 53, p. 41–71, https://doi.org/10.1016/0375-6742(94)00034-9.

Noble, D.C., Korringa, M.K., Hedge, C.E., and Riddle, G.O., 1972, Highly differentiated subalkaline rhyolite from Glass Mountain, Mono County, California: Geological Society of America Bulletin, v. 83, p. 1179–1184, https://doi.org/10.1130/0016-7606(1972)83[1179:HDSRFG]2.0.CO;2.

Noble, D.C., Rigot, W.L., and Bowman, H.R., 1979, Rare-earth-element content of some highly differentiated ash-flow tuffs and lavas, *in* Chapin, C.E., and Elston, W.E., eds., Ash-Flow Tuffs: Geological Society of America Special Paper 180, p. 77–86, https://doi.org/10.1130/SPE180-p77.

Norris, G., Jarzen, D.M., and Awai-Thorne, B.V., 1975, Evolution of the Cretaceous terrestrial palynoflora in western Canada, *in* Caldwell, W.G., ed., The Cretaceous System in the Western Interior of North America: Geological Association of Canada Special Paper 13, p. 333–364.

Nowicki, T., Crawford, B., Dyck, D., Carlson, J., McElroy, R., Oshust, P., and Helmstaedt, H., 2004, The geology of kimberlite pipes of the Ekati property, Northwest Territories, Canada: Lithos, v. 76, p. 1–27, https://doi.org/10.1016/j.lithos.2004.03.020.

Pagani, M., Huber, M., Liu, Z., Bohaty, S.M., Henderiks, J., Sijp, W., Krishnan, S., and DeConto, R.M., 2011, The role of carbon dioxide during the onset of Antarctic glaciation: Science, v. 334, p. 1261–1264, https://doi.org/10.1126/science.1203909.

Paton, C., Woodhead, J.D., Hellstrom, J.C., Hergt, J.M., Greig, A., and Maas, R., 2010, Improved laser ablation U-Pb zircon geochronology through robust downhole fractionation correction: Geochemistry, Geophysics, Geosystems, v. 11, https://doi.org/10.1029/2009GC002618.

Paton, C., Hellstrom, J., Paul, B., Woodhead, J., and Hergt, J., 2011, Iolite: Freeware for the visualisation and processing of mass spectrometric data: Journal of Analytical Atomic Spectrometry, v. 26, p. 2508–2518, https://doi.org/10.1039/c1ja10172b.

Pearson, D.L., 1984, Pollen/spore color "standard," version 2: Bartlesville, Oklahoma, Phillips Petroleum Company, Geology Branch, 3 p.

Pease, V., Miller, E., Wyld, S.J., Sokolov, S., Akinin, V., and Wright, J.E., 2018, U-Pb zircon geochronology of Cretaceous arc magmatism in eastern Chukotka, NE Russia, with implications for Pacific plate subduction and the opening of the Amerasia Basin, *in* Pease, V., and Coakley, B., eds., Circum-Arctic Lithosphere Evolution: Geological Society, London, Special Publication 460, p. 159–182, https://doi.org/10.1144/SP460.14.

Petrus, J.A., and Kamber, B.S., 2012, VizualAge: A novel approach to laser ablation ICP-MS U-Pb geochronology data reduction: Geostandards and Geoanalytical Research, v. 36, p. 247–270, https://doi.org/10.1111/j.1751-908X.2012.00158.x.

Pisera, A., Siver, P.A., and Wolfe, A.P., 2013, A first account of freshwater Potamolepid sponges (Demospongiae, Spongillina, Potamolepidae) from the middle Eocene: Biogeographic and paleoclimatic implications: Journal of Paleontology, v. 87, p. 373–378, https://doi.org/10.1666/12-079.1.

Portnyagin, M.V., Ponomareva, V.V., Zelenin, E.A., Bazanova, L.I., Pevzner, M.M., Plechova, A.A., Rogozin, A.N., and Garbe-Schönberg, D., 2020, TephraKam: Geochemical database of glass compositions in tephra and welded tuffs from the Kamchatka volcanic arc (northwestern Pacific): Earth System Science Data, v. 12, p. 469–486, https://doi.org/10.5194/essd-12-469-2020.

Ren, M., Parker, D.F., and White, J.C., 2003, Partitioning of Sr, Ba, Rb, Y, and LREE between plagioclase and peraluminous silicic magma: The American Mineralogist, v. 88, p. 1091–1103, https://doi.org/10.2138/am-2003-0718.

Ricketts, B.D., 1994, Basin Analysis, Eureka Sound Group, Axel Heiberg and Ellesmere Islands, Canadian Arctic Archipelago: Geological Survey of Canada Memoir 439, 119 p., https://doi.org/10.4095/194814.

Ring, S.J., Mutz, S.G., and Ehlers, T.A., 2022, Cenozoic proxy constraints on Earth system sensitivity to greenhouse gases: Paleoceanography and Paleoclimatology, v. 37, https://doi.org/10.1029/2021PA004364.

Sabel, M., Bechtel, A., Püttmann, W., and Hoernes, S., 2005, Palaeoenvironment of the Eocene Eckfeld maar lake (Germany): Implications from geochemical analysis of the oil shale sequence: Organic Geochemistry, v. 36, p. 873–891, https://doi.org/10.1016/j.orggeochem.2005.01.001.

Sandhu, A.S., and Westgate, J.A., 1995, The correlation between reduction in fission-track diameter and areal track density in volcanic glass shards and its application in dating tephra beds: Earth and Planetary Science Letters, v. 131, p. 289–299, https://doi.org/10.1016/0012-821X(95)00022-5.

Sarkar, C., Heaman, L.M., and Pearson, D.G., 2015, Duration and periodicity of kimberlite volcanic activity in the Lac de Gras kimberlite field, Canada and some recommendations for kimberlite geochronology: Lithos, v. 218–219, p. 155–166, https://doi.org/10.1016/j.lithos.2015.01.017.

Schaltegger, U., Ovtcharova, M., Gaynor, S.P., Schoene, B., Wotzlaw, J.-F., Davies, J.F.H.L., Farina, F., Greber, N.D., Szymanowski, D., and Chelle-Michou, C., 2021, Long-term repeatability and interlaboratory reproducibility of high-precision ID-TIMS U-Pb geochronology: Journal of Analytical Atomic Spectrometry, v. 36, p. 1466–1477, https://doi.org/10.1039/D1JA00116G.

Schandl, E.S., and Gorton, M.P., 2002, Application of high field strength elements to discriminate tectonic settings in VMS environments: Economic Geology, v. 97, p. 629–642, https://doi.org/10.2113/gsecongeo.97.3.629.

Schindlbeck, J.C., Kutterolf, S., Freundt, A., Eisele, S., Wang, K.-L., and Frische, M., 2018, Miocene to Holocene marine tephrostratigraphy offshore northern Central America and southern Mexico: Pulsed activity of known volcanic complexes: Geochemistry, Geophysics, Geosystems, v. 19, p. 4143–4173, https://doi.org/10.1029/2018GC007832.

Schröder-Adams, C., 2014, The Cretaceous Polar and Western Interior seas: Paleoenvironmental history and paleoceanographic linkages: Sedimentary Geology, v. 301, p. 26–40, https://doi.org/10.1016/j.sedgeo.2013.12.003.

Schröder-Adams, C.J., Cumbaa, S.L., Bloch, J., Leckie, D.A., Craig, J., Seif El-Dein, S.A., Simons, D.-J.H.A.E., and Kenig, F., 2001, Late Cretaceous (Cenomanian to Campanian) paleoenvironmental history of the Eastern Canadian margin of the Western Interior Seaway: Bonebeds and anoxic events: Palaeogeography, Palaeoclimatology, Palaeoecology, v. 170, p. 261–289, https://doi.org/10.1016/S0031-0182(01)00259-0.

Schmieder, M., Kennedy, T., Jourdan, F., Buchner, E., and Reimold, W., 2018, A high-precision $^{40}Ar/^{39}Ar$ age for the Nördlinger Ries impact crater, Germany, and implications for the accurate dating of terrestrial impact events: Geochimica et Cosmochimica Acta, v. 220, p. 146–157, https://doi.org/10.1016/j.gca.2017.09.036.

Scott Smith, B.H., 2008, Canadian kimberlites: Geological characteristics relevant to emplacement: Journal of Volcanology and Geothermal Research, v. 174, p. 9–19, https://doi.org/10.1016/j.jvolgeores.2007.12.023.

Scott Smith, B.H., and McKinlay, T., 2002, Emplacement of the Hardy Lake kimberlites, NWT, Canada [abstract]: Geological Association of Canada/Mineralogical Association of Canada Meeting in Saskatoon, Saskatchewan, v. 106, p. 106.

Seward, D., and Kohn, B.P., 1997, New zircon fission-track ages from New Zealand Quaternary tephra: An interlaboratory experiment and recommendations for the determination of young ages: Chemical Geology, v. 141, p. 127–140, https://doi.org/10.1016/S0009-2541(97)00086-7.

Simonetti, A., Heaman, L.M., Hartlaub, R.P., Creaser, R.A., MacHattie, T.G., and Böhm, C., 2005, U-Pb zircon dating by laser ablation-MC-ICP-MS using a new multiple ion counting Faraday collector array: Journal of Analytical Atomic Spectrometry, v. 20, p. 677–686, https://doi.org/10.1039/b504465k.

Siver, P.A., 2015, *Mallomonas schumachii* sp. nov., a fossil synurophyte bearing large scales described from an Eocene maar lake in Northern Canada: Nova Hedwigia, v. 101, p. 285–298, https://doi.org/10.1127/nova_hedwigia/2015/0270.

Siver, P.A., 2022, The downsizing of gigantic scales and large cells in the genus *Mallomonas* (Synurales, Chrysophyceae): Scientific Reports, v. 12, 4896, https://doi.org/10.1038/s41598-022-09006-1.

Siver, P.A., and Lott, A.M., 2023, History of the Giraffe Pipe locality inferred from microfossil remains: A thriving freshwater ecosystem near the Arctic Circle during the warm Eocene: Journal of Paleontology, v. 97, p. 271–291, https://doi.org/10.1017/jpa.2022.101.

Siver, P.A., and Velez, M.I., 2023, The oldest raphe-bearing diatoms: Evidence from the Upper Cretaceous of western and northern Canada: Cretaceous Research, v. 144, https://doi.org/10.1016/j.cretres.2022.105456.

Siver, P.A., Wolfe, A.P., and Edlund, M.B., 2016, *Fideliacyclus wombatiensis* gen. et sp. nov.—A Paleocene non-marine centric diatom from northern Canada with complex frustule architecture: Diatom Research, v. 31, p. 397–408, https://doi.org/10.1080/0269249X.2016.1256351.

Siver, P.A., Wolfe, A.P., Edlund, M.B., Sibley, J., Hausman, J., Torres, P., and Lott, A.M., 2019, *Aulacoseira giraffensis* (*bacillariophyceae*), a new diatom species forming massive populations in an Eocene lake: Plant Ecology and Evolution, v. 152, p. 358–367, https://doi.org/10.5091/plecevo.2019.1586.

Sláma, J., et al., 2008, Plešovice zircon—A new natural reference material for U-Pb and Hf isotopic microanalysis: Chemical Geology, v. 249, p. 1–35, https://doi.org/10.1016/j.chemgeo.2007.11.005.

Smith, K.T., Schaal, S.F.K., and Habersetzer, J., eds., 2018, MESSEL—An Ancient Greenhouse Ecosystem: Stutt gart, Germany, Senckenberg, 355 p.

Spicer, R.A., and Herman, A.B., 2010, The Late Cretaceous environment of the Arctic: A quantitative reassessment based on plant fossils: Palaeogeography, Palaeoclimatology, Palaeoecology, v. 295, p. 423–442, https://doi.org/10.1016/j.palaeo.2010.02.025.

Stacey, J.S., and Kramers, J.D., 1975, Approximation of terrestrial lead isotope evolution by a two-stage model: Earth and Planetary Science Letters, v. 26, p. 207–221, https://doi.org/10.1016/0012-821X(75)90088-6.

Stanley, E.A., 1970, The stratigraphical, biogeographical, paleoautecological and evolutionary significance of the fossil pollen group Triprojectacites: Bulletin of the Georgia Academy of Science, v. 28, p. 1–44.

Staplin, F.L., 1969, Sedimentary organic matter, organic metamorphism, and oil and gas occurrence: Bulletin of Canadian Petroleum Geology, v. 17, p. 47–66.

Stasiuk, L.D., Sweet, A.R., and Issler, D.R., 2002, Organic Petrology, Organic Geochemistry, Palynology and Petrophysics Data from Lac de Gras Kimberlites and Associated Sedimentary Rocks and Xenoliths: Geological Survey of Canada Open File 4272, https://doi.org/10.4095/213531.

Stasiuk, L.D., Sweet, A.R., Issler, D.R., Kivi, K., Lockhart, G.D., and Dyck, D.R., 2003, Pre- and post-kimberlite emplacement thermal history of Cretaceous and Tertiary sediments, Lac de Gras, Northwest Territories, Canada: International Kimberlite Conference, Extended Abstracts, v. 8, p. 1–5, https://doi.org/10.29173/ikc3014.

Stasiuk, L.D., Sweet, A.R., and Issler, D.R., 2006, Reconstruction of burial history of eroded Mesozoic strata using kimberlite shale xenoliths, volcaniclastic and crater facies, Northwest Territories, Canada: International Journal of Coal Geology, v. 65, p. 129–145, https://doi.org/10.1016/j.coal.2005.04.011.

Stiefenhofer, J., and Farrow, D.J., 2003, Crater deposits of the Mwadui kimberlite: International Kimberlite Conference, Extended Abstracts, v. 8, https://doi.org/10.29173/ikc3094.

Suan, G., et al., 2017, Subtropical climate conditions and mangrove growth in Arctic Siberia during the early Eocene: Geology, v. 45, p. 539–542, https://doi.org/10.1130/G38547.1.

Sun, S.-s., and McDonough, W.F., 1989, Chemical and isotopic systematics of oceanic basalts: Implications for mantle composition and processes, *in* Saunders, A.D., and Norry, M.J., eds., Magmatism in the Ocean Basins: Geological Society, London, Special Publication 42, p. 313–345, https://doi.org/10.1144/GSL.SP.1989.042.01.19.

Sweet, A.R., 1978, Palynology of the lower part, type section, Tent Island Formation, Yukon Territory, *in* Blackadar, R.G., Griffin, P.J., Dumych, H., and Neale, E.R.W., eds., Current Research, Part B: Geological Survey of Canada Paper 78-1B, p. 31–37.

Sweet, A.R., Ricketts, B.D., Cameron, A.R., and Norris, D.K., 1989, An integrated analysis of the Brackett Coal Basin, Northwest Territories, *in* Current Research, Part G: Geological Survey of Canada Paper 89-1G, p. 85–99.

Sweet, A.R., Stasiuk, L.D., Nassichuk, W.W., Catunneau, O., and McIntyre, D.J., 2003, Paleontology and diamonds: Geological environments associated with kimberlite emplacement, Lac de Gras, Northwest Territories, Canada: International Kimberlite Conference, Extended Abstracts, v. 8, p. 1–5.

Takahashi, K., 1974, Palynology of the upper Aptian Tanohata Formation of the Miyako Group, Northeast Japan: Pollen et Spores, v. 16, p. 535–564.

Tikhomirov, P.L., Kalinina, E.A., Moriguti, T., Makishima, A., Kobayashi, K., Cherepanova, I.Y., and Nakamura, E., 2012, The Cretaceous Okhotsk–Chukotka Volcanic Belt (NE Russia): Geology, geochronology, magma output rates, and implications on the genesis of silicic LIPs: Journal of Volcanology and Geothermal Research, v. 221–222, p. 14–32, https://doi.org/10.1016/j.jvolgeores.2011.12.011.

Tovey, M., Giuliani, A., Phillips, D., Pearson, D.G., Sarkar, C., Nowicki, T., and Carlson, J., 2021, The spatial and temporal evolution of primitive melt compositions within the Lac de Gras kimberlite field, Canada: Source evolution vs lithospheric mantle assimilation: Lithos, v. 392–393, https://doi.org/10.1016/j.lithos.2021.106142.

Traverse, A., 2007, Production, Dispersal, Sedimentation and Taphonomy of Spores/Pollen in Relation to the Interpretation of Palynofloras, *in* Traverse, A., Paleopalynology: Springer, Topics in Geobiology 28, p. 497–542, https://doi.org/10.1007/978-1-4020-5610-9_17.

Vermeesch, P., 2018, IsoplotR: A free and open toolbox for geochronology: Geoscience Frontiers, v. 9, p. 1479–1493, https://doi.org/10.1016/j.gsf.2018.04.001.

Vermeesch, P., 2021, Maximum depositional age estimation revisited: Geoscience Frontiers, v. 12, p. 843–850, https://doi.org/10.1016/j.gsf.2020.08.008.

West, C., Greenwood, D., and Basinger, J., 2019, The late Paleocene to early Eocene Arctic megaflora of Ellesmere islands, Nunavut, Canada: Palaeontographica Abteilung B, v. 300, p. 47–163, https://doi.org/10.1127/palb/2019/0066.

Westgate, J.A., 1989, Isothermal plateau fission-track ages of hydrated glass shards from silicic tephra beds: Earth and Planetary Science Letters, v. 95, p. 226–234, https://doi.org/10.1016/0012-821X(89)90099-X.

Westgate, J.A., 2015, Volcanic Glass (Fission Track), Encyclopedia of Scientific Dating Methods, *in* Jack Rink, W., and Thompson, J.W., eds., Encyclopedia of Scientific Dating Methods: Springer, p. 941–946, https://doi.org/10.1007/978-94-007-6304-3_60.

Westgate, J.A., and Bray, C.J., 2021, Glass fission-track ages, composition, and origin of tephra beds in the Upper Cretaceous Kanguk Formation, Banks Island, Arctic Canada: Canadian Journal of Earth Sciences, v. 58, p. 1233–1251, https://doi.org/10.1139/cjes-2021-0031.

Widmann, P., Davies, J.H., and Schaltegger, U., 2019, Calibrating chemical abrasion: Its effects on zircon crystal structure, chemical composition and U-Pb age: Chemical Geology, v. 511, p. 1–10, https://doi.org/10.1016/j.chemgeo.2019.02.026.

Williams, I.S., 1997, U-Th-Pb geochronology by ion microprobe: Reviews in Economic Geology, v. 7, no. 1, p. 1–35, https://doi.org/10.5382/Rev.07.01.

Wolfe, A.P., Csank, A.Z., Reyes, A.V., McKellar, R.C., Tappert, R., and Muehlenbachs, K., 2012, Pristine early Eocene wood buried deeply in kimberlite from northern Canada: PLoS One, v. 7, https://doi.org/10.1371/journal.pone.0045537.

Wolfe, A.P., Reyes, A.V., Royer, D.L., Greenwood, D.R., Doria, G., Gagen, M.H., Siver, P.A., and Westgate, J.A., 2017, Middle Eocene CO_2 and climate reconstructed from the sediment fill of a subarctic kimberlite maar: Geology, v. 45, p. 619–622, https://doi.org/10.1130/G39002.1.

Wong, T.E., Cui, Y., Royer, D.L., and Keller, K., 2021, A tighter constraint on Earth-system sensitivity from long-term temperature and carbon-cycle observations: Nature Communications, v. 12, 3173, https://doi.org/10.1038/s41467-021-23543-9.

Yorath, C.J., and Cook, D.G., 1981, Cretaceous and Tertiary Stratigraphy and Paleogeography, Northern Interior Plains, District of Mackenzie: Geological Survey of Canada Memoir 398, 76 p., https://doi.org/10.4095/109299.

Zachos, J.C., Dickens, G.R., and Zeebe, R.E., 2008, An early Cenozoic perspective on greenhouse warming and carbon-cycle dynamics: Nature, v. 451, p. 279–283, https://doi.org/10.1038/nature06588.

Zhu, J., Poulsen, C.J., and Tierney, J.E., 2019, Simulation of Eocene extreme warmth and high climate sensitivity through cloud feedbacks: Science Advances, v. 5, https://doi.org/10.1126/sciadv.aax1874.

Zonneveld, J.-P., Kjarsgaard, B.A., Harvey, S.E., Heaman, L.M., McNeil, D.H., and Marcia, K.Y., 2004, Sedimentologic and stratigraphic constraints on emplacement of the Star Kimberlite, east–central Saskatchewan: Lithos, v. 76, p. 115–138, https://doi.org/10.1016/j.lithos.2004.03.043.

Science Editor: Mihai Ducea
Associate Editor: M. Smith

Manuscript Received 4 August 2023
Revised Manuscript Received 30 November 2023
Manuscript Accepted 18 January 2024